Retromer oligomerization drives SNX-BAR coat assembly and membrane constriction

Navin Gopaldass[1], Maria Giovanna De Leo[1], Thibault Courtellemont[1], Vincent Mercier[2], Christin Bissig[1], Aurélien Roux[2,3] and Andreas Mayer[1§]

[1]Department of Immunobiology, University of Lausanne, Epalinges, Switzerland.

[2]Department of Biochemistry, University of Geneva, Geneva, Switzerland.

[3]Swiss National Centre for Competence in Research Program Chemical Biology, Geneva, Switzerland.

[§]Corresponding author: andreas.mayer@unil.ch

Abstract

Many proteins exit from endosomes through tubular carriers coated by retromer, a complex that impacts cellular signaling, lysosomal biogenesis, and numerous diseases. Retromer (CSC in yeast) forms coats by interconnecting sorting nexins (SNX). The coat performs work to deform the membrane and overcome endosomal membrane tension. To explore the dynamics of this process and the sources of the driving force, we analyzed formation of CSC/SNX-BAR retromer coats on oriented synthetic lipid tubules. CSC/SNX-BARs oligomerize bidirectionally, forming a static tubular coat that does not exchange subunits. High concentrations of SNX-BARs alone constrict membrane tubes to an invariant radius of 19 nm. At lower concentrations, CSC-complexes must drive constriction through their oligomerization. Then, CSCs populate the SNX-BAR layer at densities that increase with the starting radius of the membrane tube, and hence with the work required for constriction. Retromer-mediated crosslinking of SNX-BARs at variable densities may thus tune the energy that the coat can generate to deform the membrane. Mutations interfering with retromer oligomerization in yeast and human cells are in accord with this model.

Introduction

Endosomes and lysosomes form a complex network of interconnected organelles of different composition and function. They exchange proteins through fusion and fission with each other and, in a more selective fashion, through endosomal transport carriers (ETCs). ETCs are tubulo-vesicular structures bulging from the limiting membrane of these organelles. The formation of ETCs comprises several steps: Cargo selection, membrane deformation, and detachment from the donor organelle through membrane fission. Alternatively, cargo can also pass between endo-lysosomal compartments through kiss-and-run, a transient fusion between two endo-lysosomal organelles followed by immediate re-fission (Solinger *et al*, 2020; Luzio *et al*, 2014). ETCs form through a variety protein coats and their interaction partners, such as the retromer, retriever and CCC complexes, ESCPE-1, sorting nexins and the WASH complex (Chen *et al*, 2019; Derivery *et al*, 2009; Gomez & Billadeau, 2009; Phillips-Krawczak *et al*, 2015; Rojas *et al*, 2007; Temkin *et al*, 2011; Lucas *et al*, 2016; Simonetti *et al*, 2022, 2019).

Retromer is a conserved tubular protein coat, which was originally defined in yeast as a stable complex that dissociates into two parts: The SNX complex, consisting of the SNX-BAR sorting nexins Vps5 and Vps17, and the peripheral CSC complex (Vps26, Vps29 and Vps35) (Seaman *et al*, 1998). In non-yeast systems, the Vps26/29/35 complex alone is referred to as retromer. It is recruited to membranes through various sorting nexins. Some of them carry BAR domains, such as the SNX-BARs Vps5 and Vps17, others do not, such as Snx3/Grd19 (Harrison *et al*, 2014; Deatherage *et al*, 2020; Strochlic *et al*, 2007; Harterink *et al*, 2011). The SNX complex (Vps5/Vps17) binds membranes via PX domains, which recognize phosphatidylinositol-3-phosphate (PI3P) (Burda *et al*, 2002), and through BAR domains, which bind highly curved membranes. The SNX complex recruits CSC, which by itself shows only weak affinity for the membrane, although it can interact with the bilayer when bound to other sorting nexins, such as Snx3 (Lucas *et al*, 2016; Purushothaman & Ungermann, 2018; Leneva *et al*, 2021; Strochlic *et al*, 2007; Deatherage *et al*, 2020). Retromer associates with numerous other factors, which are important for the formation of the transport carriers and/or their fission from the membrane. These include components of the Rab-GTPase system (Seaman *et al*, 2009; Rojas *et al*, 2008; Jia *et al*, 2016; Balderhaar *et al*, 2010; Liu *et al*, 2012; Purushothaman &

Ungermann, 2018), the actin-regulating WASH complex (Harbour *et al*, 2012; Chen *et al*, 2019; Derivery *et al*, 2009; Jia *et al*, 2012; Gomez & Billadeau, 2009; Phillips-Krawczak *et al*, 2015; Temkin *et al*, 2011; Lucas *et al*, 2016), or EHD1, an ATPase that has structural similarities to dynamins (Daumke *et al*, 2007; Gokool *et al*, 2007).

Structural studies of sorting nexins and retromer begin to elucidate how these coats wrap around membranes and how they recruit cargo (Leneva *et al*, 2021; Kovtun *et al*, 2018; Hierro *et al*, 2007; Lucas *et al*, 2016; Kendall *et al*, 2020; Collins *et al*, 2005, 2008; Purushothaman *et al*, 2017; Zhang *et al*, 2021; Kendall *et al*, 2022). A further mechanistic analysis of the formation of ETCs and their fission from endo-lysosomal compartments will, however, require complementing dynamic data from in vitro systems that reproduce the formation and fission of ETCs in a well-defined, tunable and optically well-resolved setting. Attempts in this direction have already been undertaken. Retromer coat produces tubules on giant unilamellar vesicles (GUVs) (Purushothaman & Ungermann, 2018; Purushothaman *et al*, 2017). Those are hard to quantify because the tubules are numerous and difficult to resolve by light microscopy. Retromer oligomerization could also be followed on supported planar lipid bilayers (Deatherage *et al*, 2020), where protein interactions can be studied extremely well. But such a system appears less apt for observing tubulation by the coat and fission.

We engaged in an in vitro characterization of retromer because our studies on membrane fission on yeast vacuoles and mammalian endosomes revealed the PROPPINs Atg18 and WIPI1, respectively, as crucial factors (Zieger & Mayer, 2012; Peters *et al*, 2004; Gopaldass *et al*, 2017; DeLeo *et al*, 2021). Atg18 integrates with CSC to form the CROP complex (Courtellemont *et al*, 2022; Marquardt *et al*, 2022) displays much more potent membrane fission activity than the PROPPIN alone. To generate a system that may allow to analyse the mechanistic relationship of CROP to retromer, we used oriented lipid tubules on glass supports (Dar *et al*, 2015). The tubules allow to quantitatively follow the formation of the coat on them, a property which we exploited for an analysis of the properties and dynamics of retromer.

Results

Supported membrane tubes (SMTs) (Dar *et al*, 2015) are individually observable tubular membranes that are immobilized and amenable to quantitative optical analysis. SMTs can be generated by liquid flow through a microfluidic chamber carrying lipid spots on its glass bottom. The flow produces arrays of parallel membrane tubes, which probably become stabilized in this orientation by occasional contacts with non-coated spots of the glass surface. Such SMTs allow to image the behavior of proteins on the tubes over extended periods of time. The tube diameters can be quantified via a low percentage of incorporated fluorescent lipidic tracers because the fluorescence per unit tube length will depend on the number of fluorescent lipids in that unit, and hence upon the radius of the tube.

CSC and SNX-BARs cooperate to constrict pre-formed membrane tubules to a uniform radius

We adapted this system to study the formation of retromer coats. To visualize SNX/CSC coat formation, an SMT array was formed on a coverslip that was covalently coated with polyethylene glycol and mounted in a flow chamber. The SMTs were labelled through 1 mol% of Texas Red DHPE and contained 5% PI3P, because this phosphoinositide is required to recruit SNX-BARs onto membranes (Yu & Lemmon, 2001; Cheever *et al*, 2001; Song *et al*, 2001). Upon addition of purified recombinant SNX complex (Vps5 and Vps17) and mClover-tagged CSC (Vps26, Vps35, Vps29^{mClover}) (Suppl. Fig. 1a, b), uniform membrane binding could be observed by spinning disc fluorescence microscopy within seconds (Fig.1a, movie 1). PI3P and SNX were necessary to recruit CSC to the tubes (Suppl. Fig. 2a). About one minute after addition of SNX and CSC^{mClover}, the mClover-signal strongly accumulated at multiple discrete sites on a tubule, suggesting that CSC was concentrating into separate protein domains (Fig. 1a, movie 1). The domains elongated over time, as visualized by kymograph analysis (Fig 1b). Co-labelling of CSC and SNX with mRuby and GFP, respectively, revealed that the zones where both CSC^{mRuby} and SNX^{GFP} were concentrated mirrored precisely zones of decreased lipid fluorescence, which were visualized through the red-fluorescing lipid Cy5.5-PE (Fig. 1c and d). The concentrations necessary for domain-formation by SNX complex and CSC varied from one preparation to another by a factor of two to three and were in general in the range of 10-25 nM. At such low concentrations, domains did not form in the absence of CSC (Fig. 1e). Domains could also be formed by SNX alone (Fig. 1f, g and h, movie 2). However, for a given preparation this always required SNX concentrations 5-10 times above those that sufficed to generate domains in the presence of CSC.

The protein-enriched domains showed a strong reduction in lipid fluorescence, suggesting that the diameter of the underlying lipid bilayer was severely reduced (Fig. 1a-c, Suppl. Fig. 2b, c). The decrease in fluorescence was not due to a change in the direct environment of the fluorescent lipid upon protein binding (Jung *et al*, 2009; Hsieh *et al*, 2012), as we could observe the same effect using alternative lipid probes, which carry the fluorophore either on the membrane surface (Texas Red DHPE, Cy5.5-PE) or inside the hydrophobic part of the bilayer (NBD-PC) (Suppl. Fig. 2b; Fig. 1c, d). Therefore, we attribute the decrease in lipid fluorescence to a reduction in the amount of lipid underneath the protein domain, i.e., to a reduction in the radius of the membrane tube.

The radius of the membrane tubes in the constricted domains could be estimated using dynamin as a reference. Dynamin constricts membrane tubes to a defined radius of 11.2 nm (Roux *et al*, 2010). The lipid fluorescence in the SMTs can thus be calibrated and their radius can be deduced (Dar *et al*, 2015) (see Material and Methods and Supplementary Fig. 3 for details). This method revealed that the radius of membrane tubes underneath domains formed by CSC/SNX was 19.1 +/- 0.6 nm (Fig. 2 a-d), and that this radius was the same for membrane tubes constricted by high concentrations of SNX alone. Domains formed by SNX alone remained competent to bind $CSC^{mClover}$ in a second incubation phase (Fig. 2e-f). However, the recruitment of $CSC^{mClover}$ had no effect on lipid fluorescence under the pre-formed domains (Fig. 2g), suggesting that the tubes maintained their radius. This invariant radius was independent of the initial radius of the non-constricted tube, both for SNX/ $CSC^{mClover}$ and for SNX-only domains (Fig. 2d). Thus, in agreement with structural studies (Kovtun *et al*, 2018; Leneva *et al*, 2021; Zhang *et al*, 2021; Kendall *et al*, 2020; Hierro *et al*, 2007; Lucas *et al*, 2016; Purushothaman *et al*, 2017), both CSC and SNX contribute to a constriction of the membrane tubes, probably by forming the retromer coat. SNX alone has membrane scaffolding activity, which defines the diameter of the coat independently of CSC, but CSC allows coat formation at lower SNX concentrations.

Retromer coats grow rapidly and bidirectionally

Cryo-EM analyses of retromer uncovered that the interface between the two Vps35 subunits of a retromer arch was asymmetric and that these subunits differed in overall

structure (Leneva *et al*, 2021). It was proposed that this asymmetry might render coat assembly directional. Since the SMTs allow to observe coat growth in real time, we tested this hypothesis. To this end we first generated small red-fluorescing constricted coats using SNX and CSC^{mRuby} complexes. After a brief wash with protein-free buffer, SNX and $CSC^{mClover}$ complexes were added (Fig. 3a to c). The green-fluorescing $CSC^{mClover}$ extended the pre-existing red-fluorescing constricted zones that had been formed by CSC^{mRuby}. The extension speed of the coat was substantial, ranging from 1 µm/min to 1.5 µm/min. This is in a similar range as the speed of dynamin polymerization (Roux *et al*, 2010). The elongation speed of this coat can also be put into perspective by comparison to the speeds of polymerization of actin tails (up to 3.6 µm/min; (Cameron *et al*, 1999)), or microtubules (10 µm/sec; (Gierke *et al*, 2010)). Based on the proposed structure of the retromer coat (Leneva *et al*, 2021; Kovtun *et al*, 2018) we estimate the observed extension speed to require the addition of approximately 10 to 15 SNX dimers per second at each end. $CSC^{mClover}$/SNX elongated the pre-existing red-fluorescing coats at both ends with similar rates (Fig. 3b and c). Thus, despite the asymmetry in the arches (Leneva *et al*, 2021), the retromer coat displayed no inherent directionality of growth.

The retromer coat is a static structure that does not exchange subunits

Structural studies of retromer-coated tubules formed with Vps5 revealed that these retromer coats are irregular in terms of their coverage with protein and that CSC oligomerizes into arch-like structures on the sorting nexins (Leneva *et al*, 2021; Kovtun *et al*, 2018). The irregularity raises several questions: Does the tubular coat represent a static structure, or is it rather dynamic, with subunits readily moving in and out? Does CSC facilitate SNX coat formation by dimerization and does the apparent variability in the occupancy of the SNX layer by CSC have functional implications?

The formation of a static structure by SNX/CSC implies that the proteins form a rigid coat that might stabilize the underlying membrane tubule. To test this, we used an assay where a membrane tubule is pulled out of a giant unilamellar vesicle (GUV) by means of an optical trap. Through analyzing the displacement of the bead in the trap, such a setup allows direct measurement of the force required to generate and maintain the tubule (Roux *et al*, 2010). Shortly after SNX/$CSC^{mClover}$ addition, protein bound the pulled tubule (Fig. 4a). As a consequence, the pulling force exerted on the bead decreased sharply (Fig 4b). Elongating this tubule by displacing the GUV transiently increased in the force again (Fig.

4c and d), but as the SNX/CSC^{mClover} coat grew along the newly extracted portion of the tubule (Fig. 4e), the force decreased again. This could be repeated several times (Fig. 4d). Together, these data suggest that the SNX/CSC coat forms a rigid scaffold that suffices to stabilizes a membrane tubule.

CSC density may define the work that the coat performs in deforming membranes

Binding of CSC adds further interactions to the SNX layer (Kovtun *et al*, 2018; Leneva *et al*, 2021; Lucas *et al*, 2016), and could hence provide additional energy for membrane scaffolding. This led us to test whether coat stoichiometry might vary as a function of the radius of the starting tubule, because constricting a less curved membrane requires more work (Roux, 2013). We first assayed whether the coats are saturated, using SNX and CSC separately in a two-stage experiment. Constricted coats on SMTs were pre-formed from red-fluorescing SNX/CSC^{mRuby} complexes. Non-bound proteins were washed away and, in a second incubation, we added either green-fluorescing SNX^{GFP} or CSC^{mClover} (Fig. 5 a, b). SNX^{GFP} was recruited to the non-constricted areas of the tubes but could not integrate into the constricted domains, suggesting that the membrane in these domains was fully covered. By contrast, CSC^{mClover} bound mainly to the constricted domains. CSC^{mClover} was not recruited in exchange for pre-bound CSC^{mRuby}, which might have dissociated from the constriction, because the CSC^{mRuby} signal in the constricted domains remained constant after the addition of CSC^{mClover} (Fig. 5c). This suggests that the constricted domains are saturated for SNX complexes but retain free binding sites for additional CSC.

To test whether the density of CSC on retromer coats has functional significance, we compared the density of CSC in constricted coats that had had been formed on membrane tubes of different starting radius. The SMT system is very apt for this analysis because it simultaneously generates many tubes of variable radii on the same slide. Calibration via the integrated fluorescent lipids showed that these "naked tube" radii varied mostly from 20-40 nm under the conditions we employed. We measured the radius of non-constricted regions to approximate the starting radius of the tube and then measured the signals of SNX^{GFP} and CSC^{mClover} in the constricted domains of that tube (Suppl. Fig. 3). Whereas CSC^{mClover} fluorescence per unit length of constricted tube increased as a function of starting tube radius (Fig. 5d, e), the density of SNX^{GFP} in the constricted domains was independent of the starting tube radius (Fig. 5f, g). Thus, the larger the starting tube, the

more CSC is incorporated into the constricted coat. Since the energy required to constrict a membrane tube to a defined diameter increases with its initial radius, this suggests that the work that the SNX coat performs to constrict the membrane may be tuned through the density of CSC complexes that are incorporated to connect them.

Retromer oligomerization supports coat constriction

CSC arches can connect multiple SNX subunits and can form oligomers (Deatherage *et al*, 2020; Kendall *et al*, 2020; Kovtun *et al*, 2018; Lucas *et al*, 2016). Oligomerization might provide additional bonds for membrane deformation by the coat and/or facilitate coat assembly by constraining the subunits in an orientation relative to each other that is best compatible with a constricted lipid tube. In both cases, the capacity of CSC to oligomerize should play an important role for driving the formation of constricted domains. Structural studies showed that CSC forms dimers through a conserved interface on Vps35 (Kendall *et al*, 2020; Leneva *et al*, 2021). To assess the contribution of retromer dimerization on coat formation we used the PDB-PISA software (https://www.ebi.ac.uk/pdbe/pisa/) to model the Vps35-Vps35 dimerization interface, using a retromer CryoEM structure (Kovtun *et al*, 2018; Leneva *et al*, 2021) as an input. PDB-PISA calculates the energy contribution of each residue to a protein-protein interaction surface. This approach predicts residues to form hydrogen bonds or salt bridges between the two Vps35 subunits. We selected the conserved Vps35 residues D671, L722 and R775 for substitution by alanine, yielding the *vps35*^{PISA} allele (Fig. 6a, b). We also generated *vps35*^{AAA3KE}, in which another set of conserved residues in the interaction region are substituted. The AAA3KE substitutions abolish the capacity of mammalian VPS35 to self-associate and lead to partial secretion of the vacuolar protease CPY in yeast (Kendall *et al*, 2020). A recent structural study showed that all these substituted residues contribute to an asymmetric Vps35-Vps35 interface (Leneva *et al*, 2021). We extracted CSC complexes containing both Vps35 variants from yeast (Fig. 6c) and tested their capacity to form higher order oligomers by blue native gel electrophoresis (Fig. 6d). CSC^{wt} migrated in three main bands at apparent molecular masses compatible with a Vps29^{mClover}-containing monomer of CSC (207 kDa), a dimer (414 kDa), and a tetramer (828 kDa). The most slowly migrating species was abolished in CSC from *vps35*^{AAA3KE} cells and weaker in CSC from *vps35*^{PISA}, while the intermediate-sized forms persisted. This suggests that the slowest form represents a CSC tetramer held

277 together by Vps35 dimerization, whereas the dimer may persist through a Vps26-Vps26
278 interface (Kovtun *et al*, 2018).
279
280 We performed SMT assays to assess the capacity of both CSC variants to form
281 constricted domains. To avoid potential influences of the CSC variants on the speed or
282 extent of SNX recruitment to the tubes, the experiments were performed in two phases. A
283 first incubation at low SNX concentration (25 nM) allowed this complex to bind the tubes
284 without forming constricted domains (Fig. 7a, b). Unbound SNX was washed away before
285 $CSC^{mClover}$ variants were added for the second incubation phase. $CSC^{mClover}$ with
286 $vps35^{AAA3KE}$ and $vps35^{PISA}$ was recruited to the prebound SNX with similar kinetics and to
287 similar extent as the wildtype complex (Fig. 7b-d). However, only wildtype CSC drove the
288 formation of constricted domains (Fig. 7 b, c). The CSC variants also failed to drive
289 constriction when they were co-incubated with SNX right from the beginning in a one-
290 phase experiment (Suppl. Fig. 4a-d). That the CSC variants were in principle able to bind a
291 constricted SNX layer was shown by a further experiment, in which constricted SNX-only
292 coats were pre-formed in a first incubation phase at high SNX concentration. $CSC^{AAA3KE-}$
293 ^{mClover} and $CSC^{PISA\text{-}mClover}$ bound to those preformed constrictions similarly as the wildtype
294 complex (Suppl. Fig. 4 e, f). Together, these results suggest that higher order self-
295 assembly of CSC via the conserved Vps35 interface is necessary to drive membrane
296 constriction by the SNX/CSC coat.
297
298 **Mutations affecting retromer oligomerization impair cargo sorting in vivo**
299
300 We used $vps35^{AAA3KE}$ and $vps35^{PISA}$ to test the relevance of CSC oligomerization in vivo.
301 To this end, VPS35 was TAP-tagged and corresponding nucleotide exchanges were made
302 at the VPS35 genomic locus, making the mutated alleles the sole source of Vps35 protein.
303 Both $vps35^{AAA3KE}$ and $vps35^{PISA}$ were expressed at similar levels as a $VPS35^{WT}$ allele.
304 (Suppl. Fig. 5a). They supported normal localization and abundance of yomCherry fusions
305 of the CSC subunit Vps29 and the SNX subunit Vps17, suggesting that they are folded
306 (Suppl. Fig. 5b and c). In contrast to an earlier study, which used secretion of the vacuolar
307 protease CPY as an indirect assay and found only a very mild impact of $vps35^{AAA3KE}$
308 (Kendall *et al*, 2020), we assessed retromer function through microscopic localization of a
309 yEGFP fusion of Vps10. Vps10 is a cargo receptor that uses retromer for returning from
310 the pre-vacuolar compartment (the equivalent of a late endosome) to the trans-Golgi

311 network (TGN) (Marcusson *et al*, 1994). Cells expressing wildtype VPS35 showed
312 Vps10^{yEGFP} mostly in small dots scattered in the cytosol or adjacent to the vacuole (Fig.
313 8a), consistent with its expected location in the TGN and pre-vacuolar compartment (Chi *et*
314 *al*, 2014). By contrast, cells lacking VPS35 (*vps35Δ*) accumulated significant amounts of
315 Vps10^{yEGFP} on the vacuolar membrane, where they co-localized with the lipidic vacuole
316 stain FM4-64 (Fig. 8a, b). This vacuolar localization is a hallmark of defective retromer
317 function in yeast. It results from the failure to recycle Vps10 from the pre-vacuolar
318 compartment before it finally fuses with the vacuole. The *vps35^{AAA3KE}* and *vps35^{PISA}* alleles
319 produced an intermediate phenotype, where vacuoles were significantly more labelled by
320 Vps10^{yEGFP} than in wildtype, but less than in *vps35Δ* (Fig. 8 a and b). The pre-vacuolar
321 compartment recruits SNX and CSC (Burda *et al*, 2002; Liu *et al*, 2012). In line with this,
322 Vps17^{yomCherry} or Vps29^{yomCherry} appeared as scattered dots when visualized by
323 fluorescence microscopy (Suppl. Fig. 5b, c). We quantified the number of Vps10^{yEGFP} dots
324 that were also Vps17^{yomCherry} positive. While 50% of Vps10^{yEGFP} positive dots in wildtype
325 cells co-localized with Vps17^{yomCherry}, 80-90% of colocalization was observed in cells
326 expressing *vps35^{AAA3KE}* or *vps35^{PISA}* (Suppl. Fig. 5d). This is consistent with Vps10 being
327 collected into SNX-containing structures but unable to recycle back to the Golgi.
328 Correlative light and electron microscopy of the Vps10^{yEGFP} dots in *vps35^{PISA}* cells showed
329 that the structures accumulating Vps17 were indeed PVCs, because they carried multiple
330 lumenal vesicles, which is characteristic for these compartments (Fig. 8c).
331
332 As a readout for retromer function in human cells, we used the glucose transporter
333 GLUT1, a well-characterized retromer cargo (Liu *et al*, 2012; Steinberg *et al*, 2013;
334 Hesketh *et al*, 2014; Kvainickas *et al*, 2017; Evans *et al*, 2020). GLUT1 is normally
335 localized at the plasma membrane and this localization requires its retromer-dependent
336 export from endosomes. Knock-down of hVPS35 in HK2 cells resulted in a strong
337 reduction of GLUT1 on the plasma membrane, consistent with a lack of its retromer-
338 dependent recycling (Fig. 9a). Expression of an siRNA resistant form of hVPS35 rescued
339 this phenotype, while expression of the corresponding mammalian mutant alleles
340 hVPS35^{AAA3KE} and hVPS35^{PISA} did not (Fig. 9b, c). Expressing the AAAKE and PISA
341 variants in wildtype cells led to a similar GLUT1 recycling phenotype as in the knock-down
342 cells, while expression of the wildtype protein did not (Suppl. Fig. 6). This dominant
343 negative effect suggests that the mutant proteins are correctly folded such that they can
344 compete with the endogenous wildtype version for retromer complex formation. Another

345 striking phenotype of cells lacking hVPS35 is an increase in the size of lysosomal
346 compartments, probably due to a lack of membrane recycling and/or accumulation of
347 undigested material resulting from insufficient delivery of lysosomal enzymes (Cui *et al*,
348 2018). hVps35 knock-down cells showed bigger LAMP1-positive lysosomal compartments
349 (Suppl. Fig. 7a). These enlarged compartments could be brought back to normal size by
350 expressing an siRNA resistant form of hVPS35, while expression of hVPS35^{PISA} and
351 hVPS35^{AAA3KE} failed to rescue this phenotype (Suppl. Fig. 7b). Altogether, these data
352 suggest a conserved role for Vps35 oligomerization in both yeast and human cells.
353
354
355 **Discussion**
356
357 Structural analyses have revealed many important features of retromer coats (Hierro *et al*,
358 2007; Lucas *et al*, 2016; Kendall *et al*, 2020; Collins *et al*, 2005, 2008; Zhang *et al*, 2021;
359 Purushothaman *et al*, 2017). Both Snx3- and Vps5-based coats show CSC forming arch-
360 like structures that interconnect the sorting nexins over more than 20 nm and angular
361 sections of around 60°C (Leneva *et al*, 2021; Kovtun *et al*, 2018). These models show
362 limited regularity of the coat, both with respect to the placement of sorting nexins and their
363 coverage with CSC (Leneva *et al*, 2021; Kovtun *et al*, 2018). This irregularity was
364 suggested to represent potential plasticity that may, for example, allow the coat to adjust to
365 different membrane curvatures or to integrate other proteins. Dynamic aspects of coat
366 assembly have, however, not yet been experimentally tested. Our analyses of retromer
367 coat formation in real time provide complementing functional information that relates to
368 several features of the structural models. In our experiments with supported membrane
369 tubes, SNX/CSC assembled into a coat that constricted membranes of variable starting
370 curvature to an invariant radius of 19 nm. This number, obtained with a coat including
371 Vps5 and Vps17, is in the range of the radius of 15 nm that was obtained in a structural
372 study of a CSC coat formed with Vps5 alone (Kovtun *et al*, 2018) and similar to the radius
373 of tubules formed by mammalian Vps5 homologs (Weering *et al*, 2012). Thus, even though
374 both yeast SNX-BAR proteins, Vps5 and Vps17, are required for retromer function
375 (Horazdovsky *et al*, 1997; Seaman & Williams, 2002), absence of one of them does not
376 have a major impact on the dimensions of the membrane tubules shaped by retromer.
377

The coat formed by SNX/CSC appears as a stable and static scaffold as no exchange between subunits was observed when preformed coats were incubated with an excess of either SNXs or CSC. Rigidity of the coat is illustrated by its ability to stabilize membrane tubules pulled out of a GUV. Similar experiments allowed to calculate the polymerization energy of dynamin by plotting membrane tension against the residual force exerted by the membrane tubule carrying the polymerized coat (Roux *et al*, 2010). We measured no significant residual force on SNX/CSC tubules in the range of membrane tension tested. This suggests a high polymerization energy of the retromer coat which, however, cannot be quantified through this assay at this point. Determining it will require much more work and is beyond the scope of this paper.

In situ, the stability of the coat and its stabilizing effect on the underlying tubule could be relevant in various ways. It might influence endosomal maturation, where efficient intralumenal vesicle formation by the ESCRT complex requires low endosomal membrane tension. Stabilization of membrane tubules through retromer might maintain the endosomal membrane under high tension, which might then suppress MVB formation as long as sufficient amounts of recycling cargo are present in the endosome. Stability of the retromer coat could also be relevant for the final detachment of a coated carrier: It may impose constraints on lipid flow beneath the coat and thereby promote friction-mediated membrane fission (Simunovic *et al*, 2017), when forces pull the tip of the membrane tubule. Such forces might be generated and transmitted through retromer-interacting proteins. In mammalian cells, the CSC interacts with the WASH complex, an activator of Arp2/3 that generates branched actin filaments. It was proposed that actin polymerization generates force to elongate the retromer coated tubule and ultimately cause its fission (Derivery *et al*, 2009; Gomez & Billadeau, 2009; Harbour *et al*, 2012; Phillips-Krawczak *et al*, 2015; Temkin *et al*, 2011; Jia *et al*, 2012). This force would be most efficiently transferred to the growing tubule through a retromer scaffold that is static and stable, which would be in line with our experimental observations. A caveat for this working model is that WASH does not exist in yeast - although also in this organism force produced by actin is harnessed to drive membrane trafficking processes, such as endocytosis (Goode *et al*, 2015; Kaksonen, 2008). One would hence have to postulate that in this system force is transmitted independently of WASH.

411 The coat radius of 19 nm can be defined by SNX alone, but CSC facilitates membrane
412 constriction at lower SNX concentration. In the constricted zones, the density of
413 occupation of SNX by CSC varies as a function of the starting diameter of the non-
414 constricted membrane tube. This suggests that constriction of less curved membranes
415 engages more CSC, resulting in a SNX coat with a higher degree of CSC-mediated
416 crosslinking between the SNX subunits. The energy provided by these additional bonds
417 and enhanced scaffolding of SNX by CSC may be two factors that enhance the capacity of
418 the coat to work on the membrane. Then, the coat need not operate at a fixed
419 stoichiometry and retromer density but can be tuned according to the circumstances. This
420 is relevant because the loading and membrane tension of endo-lysosomal compartments
421 can be altered by a multitude of processes, such as solute transport, membrane influx
422 (transport vesicles, autophagy), or the formation of intralumenal vesicles (Saric &
423 Freeman, 2020; Chadwick *et al*, 2021; Scott *et al*, 2014). Tubulation requires more work at
424 higher membrane tension, which could be provided by forming a coat with higher CSC
425 content. Elevated CSC density should also offer more binding sites for WASH and might
426 thereby enhance force transmission by actin on the growing tubule. Regulating the
427 concentration of active CSC could thereby allow the cell to tune retromer-mediated
428 membrane exit from endosomes to operate in a wide range of endosomal membrane
429 tension.
430
431 CSC incorporation into the coat may provide additional force for tubule formation. That this
432 contribution depends on CSC oligomerization is underscored by the effect of substitutions
433 in the conserved Vps35-Vps35 interface, which compromise oligomerization (Kendall *et al*,
434 2020; Leneva *et al*, 2021). They abolish the capacity of CSC to drive membrane
435 constriction, lead to miss-sorting of the retromer-dependent cargo receptor Vps10 in yeast,
436 and, probably therefore, to the observed partial secretion of the vacuolar peptidase CPY
437 (Kendall *et al*, 2020). We did not test the ability of human hVPS35^{AAA3KE} or hVPS35^{PISA} to
438 form a stable coat in vitro, but these variants induced a strong and even dominant negative
439 recycling defect of the retromer cargo GLUT1 in living cells. This points to a conserved role
440 of Vps35-mediated retromer oligomerization in protein recycling from endosomes.
441
442 The asymmetry of the Vps35-Vps35 interface was proposed to have potential functional
443 consequences, such as for binding cofactors to the arch in a 1:2 stoichiometry and/or
444 conferring directionality to the growth of the coat (Leneva *et al*, 2021). In our experiments,

445 the coat grew bidirectionally, suggesting that it lacks an inherent preference for adding new
446 subunits at one end. It remains possible, however, that directionality of coat growth can be
447 conferred by additional factors that have not been present in our in vitro system. Structural
448 asymmetry might also be exploited for other purposes, for example for binding cargo such
449 as Vps10, which was proposed to bind to the C-terminal part of Vps35 (Nothwehr *et al*,
450 1999) and promotes the tubulation activity of SNX/CSC coats (Purushothaman &
451 Ungermann, 2018). Cargo exerting control over tubule formation through CSC recruitment
452 might then ensure that the recycling machinery is activated when needed.
453
454
455
456
457
458

459 **Material and methods**

460

461 **Materials**

462 The following lipids were purchased from Avanti Polar Lipids (USA): Egg L-alpha-
463 phosphatidylcholine (EPC); 1,2-dioleoyl-sn-glycero-3-phospho-L-serine sodium salt
464 (DOPS); 1,2-dioleoyl-sn-glycero-3-phospho-(1'-myo-inositol-3'-phosphate) (PI3P); 1,2-
465 dioleoyl-sn-glycero-3-phosphoethanolamine-N-(Cyanine 5.5) (Cy5.5 PE); 1-Oleoyl-2-[12-
466 [(7-nitro-2-1,3-benzoxadiazol-4-yl)amino]dodecanoyl]-sn-Glycero-3-Phosphocholine (NBD-
467 PC). All lipids were dissolved in chloroform. Phosphatidylinositol phosphates were
468 dissolved in chloroform/methanol/water (20:10:1). Texas red DHPE (Thermofisher cat.
469 T1395MP) was purchased as a mixed isomer. The para isomer was separated by thin
470 layer chromatography as previously described (Dar *et al*, 2015).

471

472 **Cell culture, strains and plasmids**

473 Yeast cells BY4742 were grown at 30°C in YPD (2% peptone, 1% yeast extract, 2% β-D-
474 glucose). Genes were deleted by replacing a complete open reading frame with a marker
475 cassette (Janke *et al*, 2004; Güldener *et al*, 1996) (see Appendix Table S1 for a list of
476 strains used in this study and Appendix Table S2 for a list of PCR primers used in this
477 study). Gene tagging was done as described (Sheff & Thorn, 2004). Strains used for
478 expression and purification of the retromer complex have been previously described
479 (Appendix Table 1). VPS35 with genomic mutations at the C-terminus were amplified by
480 PCR from a synthetic gene corresponding to the last 1000 bp of VPS35 for the PISA
481 mutant, or from the pRS315-Vps35AAA3KE plasmid (Kendall *et al*, 2020) for the AAA3KE
482 mutant. These fragments were then fused to a LEU2 cassette by fusion PCR and
483 transformed into yeast cells (Janke *et al*, 2004)

484

485 **Live microscopy**

486 Vacuoles were stained with FM4-64 essentially as described (Desfougères *et al*, 2016). An
487 overnight preculture in HC (Hartwell's complete) medium was used to inoculate a 10 ml
488 culture. Cells were then grown in HC to an OD_{600} between 0.6 and 1.0. The culture was
489 diluted to an OD_{600} of 0.4, and FM4-64 was added to a final concentration of 10 μM from a
490 10 mM stock in DMSO. Cells were labelled for 60 min with FM4-64, washed three times in
491 fresh media by short and gentle centrifugation in a benchtop centrifuge, and then
492 incubated for 60 min in media without FM4-64. Right before imaging, cells were

493 concentrated by a brief low-speed centrifugation, resuspended in 1/10 of their supernatant,
494 placed on a glass microscopy slide and overlaid with a 0.17 mm glass coverslip. Imaging
495 was done with a NIKON Ti2 spinning disc confocal microscope with a 100x 1.49 NA lens.
496 Z-stacks were taken with a spacing of 0.3 µm and assembled into maximum projections.
497 Image analysis was performed with ImageJ. Pearson's correlation coefficient was used to
498 quantify the colocalization between Vps10 and FM4-64. The Nikon NIS-Elements Software
499 Pearson's correlation tool was used on at least 5 single stacks containing at least 100 cells
500 each. All performed experiments were repeated at least three times. SEM calculation and
501 potting were done with Graphpad PRISM software.
502
503 **Protein purification**
504 TAP-tagged retromer complex was extracted from yeast as previously described
505 (Purushothaman *et al*, 2017; Purushothaman & Ungermann, 2018). Briefly, a 50 mL
506 preculture of cells was grown over night to saturation in YPGal medium. The next day, two
507 1L cultures in YPGal were inoculated with 15 mL of preculture and grown for 20 h to late
508 log phase (OD_{600} = 2 to 3). All following steps were performed at 4°C. Cells were pelleted
509 and washed with 1 pellet volume of cold RP buffer (retromer purification buffer: 50 mM Tris
510 pH 8.0, 300 mM NaCl, 1 mM $MgCl_2$, 1 mM PMSF, Roche complete protease inhibitor).
511 Pellets were either processed immediately or flash-frozen in liquid nitrogen and stored at -
512 80°C. For cell lysis, the pellet was resuspended in one volume of RP buffer and passed
513 through a French press (One shot cell disruptor, Constant Systems LTD, Daventry, UK) at
514 2.2 Kpsi. 1 mg DNAse I was added to the lysate followed by a 20 min incubation on a
515 rotating wheel. The lysate was precleared by centrifugation for 30 min at 45'000 xg in a
516 Beckman JLA 25.50 rotor and cleared by a 60 min centrifugation at 150'000 xg in a
517 Beckman Ti60 rotor. The cleared supernatant was passed through a 0.2 µm filter and
518 transferred to a 50 mL Falcon tube. 1 mL IgG bead suspension (GE Healthcare, cat 17-
519 0969-01) was washed three times with RP buffer and added to the supernatant. After 60
520 min incubation on a rotating wheel, beads were spun down and washed 3 times with RP
521 buffer. 250 µg of purified HIS-TEV protease from E. coli was added to the beads. After 30
522 min incubation at 4°C, beads were centrifuged, the supernatant containing purified
523 retromer subcomplex was collected and concentrated on a 100 kDa cutoff column
524 (Pierce™ Protein Concentrator PES, 100K MWCO). The concentrated protein fraction was
525 re-diluted in RP buffer and reconcentrated 3 times. This final step allowed for removal of
526 TEV protease and a high enrichment for intact complexes. Proteins were concentrated to

527 ~2 mg/mL, aliquoted in 10 µL fractions and flash-frozen in liquid nitrogen. Proteins were
528 stored at -80°C and used within 3 months. Thawed aliquots were used only once.
529
530 **Supported membrane tubes**
531 Supported membrane tubes were generated as described (Dar *et al*, 2015).
532 Briefly, glass coverslips were first washed with 3 M NaOH for 5 min and rinsed with water
533 before a 60 min treatment with piranha solution (95% H_2SO_4 / 30% H_2O_2 3:2 v/v).
534 Coverslips were rinsed with water and dried on a heat block at 90°C. Coverslips were then
535 silanized with 3-glycidyloxypropyltrimethoxysilane (Catalogue no. 440167, Sigma) for 5 h
536 under vacuum, rinsed with acetone and dried. Polyethylene glycol coating was done by
537 placing the coverslips in a beaker containing PEG400 (Sigma) at 90°C for 60 h. Coverslips
538 were washed with distilled water and stored for up to 2 months at room temperature in a
539 closed container.
540 To generate supported membrane tubes, lipids were mixed from 10 mg/mL stocks in a
541 glass vial and diluted to a final concentration of 1 mg/mL in chloroform. The same lipid mix
542 was used throughout this study (5% PI(3)P, 15% DOPS, 0.1% fluorescent lipid tracer (in
543 most cases Texas red DHPE), 79.5% egg-PC). Lipids were then spotted (typically 1 µL,
544 corresponding to about 1 nmol) on the coverslips and dried for 30 min under vacuum. The
545 coverslip was mounted on an IBIDI 6-channel µ-slide (µ-Slide VI 0.4. IBIDI, catalog no:
546 80606). Lipids were hydrated for 15 min with buffer (PBS) and SMTs were generated by
547 injecting PBS into the chamber using an Aladdin Single-Syringe Pump (World Precision
548 Instruments, model n°. AL-1000) at a flow rate of 1,5 mL/min for 5 min. SMTs were left to
549 stabilize without flow for 5 min before the start of the experiment. Protein stocks (typically
550 1-2 µM) were first diluted in PBS and then injected in the chamber at a flow rate of 80 µL
551 per minute. Tubes were imaged with a NIKON Ti2 spinning disc confocal microscope
552 equipped with a 100x 1.49 NA objective.
553
554 **Native-PAGE, SDS-PAGE and Western blotting**
555 For analysis of CSC oligomer formation, 10 µL of purified CSC (~2 mg/mL) were diluted
556 1:1 with water and incubated for 5 min at 25°C. Samples were run on a commercial native-
557 PAGE gel (3 to 12%, Bis-Tris, 1.0 mm, Mini Protein Gel, 10-well, Invitrogen, Cat.
558 BN1001BOX) at 100 V tension using as running buffer 50 mM BisTris, 50mM Tricine, pH
559 6.8 (Invitrogen number BN2007). Cathode buffer: running buffer + 1/200 0.4% Coomassie
560 G-250. Sample buffer: 50 mM BisTris, 6 N HCl, 50 mM NaCl, 10% w/v Glycerol, 0.001%

561 Ponceau S, pH 7.2). Gels were run at 4° C. After the run, gels were then washed in 20%
562 ethanol + 10% acetic acid for 2 hours.
563
564 **Quantifcation of SMT fluorescence**
565 SMT fluorescence was quantified with ImageJ. Line scan analysis was performed along
566 tubules using an ImageJ plugin (available as a txt file in the supplement; see also Suppl.
567 Fig.2). Each line scan was performed perpendicular to the tubule. Scans were made along
568 the tubule with a one-pixel increment. For each line scan, a Gaussian curve was fitted, and
569 the maximum height was extracted. Maximum height was then plotted against the tube
570 length for all channels. For quantification of the diameters of the tubes, lipid fluorescence
571 values of a tubule underneath a constricted protein domain, extracted from the series of
572 line scans described above, was sorted in ascending order. The curve typically showed
573 two plateaus, the lower corresponding to the constricted state and the higher to the non-
574 constricted one. Plotting the corresponding GFP values confirmed that the GFP-labelled
575 protein localized to the constricted zone. For each tube, the zones corresponding to the
576 constricted and non-constricted areas were determined manually and the mean
577 fluorescence value was used to calculate the tube diameter. Tube diameter was calibrated
578 as described (Dar *et al*, 2015) using purified human ΔPRD-dynamin-1 (Colom *et al*, 2017)
579 as a reference.
580
581 **Tube Pulling**
582 The experimental set-up used to aspirate GUVs with a micropipette and pull a membrane
583 tube was the same as previously reported (Chiaruttini *et al*, 2015) combines bright-field
584 imaging, spinning disc confocal microscopy and optical tweezers on an inverted Nikon
585 Eclipse Ti microscope. GUVs were made by electro-formation as described (Angelova *et*
586 *al*, 1992). Briefly, lipid mix (the same mix as for SMT experiments, supplemented with
587 0.03% mol/mol of the biotinylated lipid DSPE-PEG2000-Biotin, Avanti Polar Lipids,
588 Alabaster, AL, USA) in chloroform was deposited on indium-titanium oxide glass slides and
589 dried for 60 min at 55°C to evaporate all solvents. GUVs were electroformed at 1 V and 10
590 Hz for 60 min at 55°C in a 380 mM sucrose solution. GUVs were then removed from the
591 chamber and placed in an Eppendorf tube until use. GUVs were used within 1–
592 2 h after formation. A GUV is aspirated within a micropipette connected to a motorized
593 micromanipulator (MP-285, Sutter Instrument, Novato, CA, USA) and a homemade
594 pressure control system (Zaber Micro linear actuator, Zaber Technologies Inc., Canada)

that sets the aspiration pressure ΔP. Then, a membrane nanotube is pulled out from the vesicle through a streptavidin-coated bead (3.05 µm diameter, Spherotec, Lake Forest, IL, USA) held in a fixed optical trap. The optical trap was custom-made with a continuous 5 W 1064 nm fiber laser (ML5-CW-P-TKS-OTS, Manlight, Lannion, France) focused through a 100X 1.3 NA oil immersion objective. The force F exerted on the bead was calculated from Hooke's law: $F = k*\Delta x$, where k is the stiffness of the trap ($k = 60$ pN.µm^{-1}) and Δx the displacement of the bead from its equilibrium position. A mix of SNXs / CSC-mClover at 1 µM with 280 mosm osmolarity was injected with a micropipette connected to a motorized micromanipulator and to the Fluigent pressure control system (MFCS-VAC, −69 mbar; Fluigent).

CLEM

CLEM was performed as described (Muriel *et al*, 2021; Kukulski *et al*, 2012). Briefly, cells of a logarithmically growing culture were concentrated by centrifugation at 3000 rpm for 2 min at RT. A few microliters of a thick cell slurry were pipetted onto a 3-mm-wide and 0.1-mm deep specimen carrier (Wohlwend type A) closed with a flat lid (Wohlwend type B). The assembled carrier sandwich was high-pressure frozen using a Wohlwend HPF Compact 02 and disassembled in liquid nitrogen. High-pressure frozen samples were processed by freeze substitution and embedding in Lowicryl HM20 using the Leica AFS 2 robot as described (Kukulski *et al*, 2012). 300 nm sections were cut with a diamond knife using a Leica ultramicrotome, collected in water and picked up on carbon-coated 200-mesh copper grids (AGS160; Agar Scientific). For light microscopy the grid was placed onto a drop of water and mounted onto a microscopy slide. Light microscopy images were acquired on a NIKON Ti2 spinning disc confocal microscope with a 100x 1.49 NA lens. The grid was recovered, dried and stained with Reynolds lead citrate for 10 min. 10-nm protein A-coupled gold beads were adsorbed to the top of the section as fiducials for tomography. TEMs were acquired on a FEI Tecnai 12 at 120 kV using a bottom mount FEI Eagle camera (4k x 4k). For tomographic reconstruction, tilt series were acquired over a tilt range of ± 60° at 1° increments using the Serial EM software. Tomogram reconstruction was performed using the IMOD software package with gold fiducial alignment.

Mammalian cell experiments

628 All chemical reagents were from Sigma-Aldrich unless specified otherwise. Other rea-
629 gents: Opti-MEM (Thermo Fischer, 11058021) and Trypsin (Thermo Fischer, 27250018);
630 LysoTracker® Deep Red (Thermo Fisher Scientific, L12492; Protease inhibitor (PI) cocktail
631 (final concentrations: 40 M pefablock SC (Merck, 11429876001), 2.1 M leupeptin (Merck,
632 11529048001), 80 μM o-phenantroline (Merck ,131377), 1.5 μM pepstatin A (Merck,
633 11524488001).
634
635 *Cell culture, transfection and treatments*
636 HK2 cells were grown in DMEM-HAM's F12 (GIBCO-Life Technologies); supplemented
637 with 5% fetal calf serum, 50 IU/mL penicillin, 50 mg/mL streptomycin, 5 µg/mL insulin, 5
638 µg/mL transferrin, 5 ng/mL selenium (LuBio Science). Cells were grown at 37°C in 5%
639 CO2 and at 98% humidity. Media, serum and reagents for tissue culture were purchased
640 from GIBCO (Invitrogen). HK2 cells were transfected with different plasmids using X-
641 tremeGENE HP DNA transfection reagent (Sigma-Aldrich) according to the manufacturer's
642 instructions. Briefly, the plasmid was diluted with Opti-MEM I Medium without serum to a
643 final concentration of 1 µg plasmid DNA /100 µl medium (0.01 µg/µl) and gently mixed.
644 Then, 3 µl of X-tremeGENE HP DNA Transfection Reagent was added directly into the
645 medium containing the diluted DNA. The transfection reagent: DNA complex was incu-
646 bated for 30 at room temperature under the hood. Finally, the transfection complex was
647 added to the cells in a dropwise manner and they were incubated 24 hours at 37°C in a
648 CO_2 incubator.
649 The HK-2 cell line was checked for mycoplasma contamination by a PCR-based method.
650 All cell-based experiments were repeated at least three times.
651
652 *Knockouts and RNA interference*
653 For RNA interference, HK2 cells were plated in 24well-plate and then transfected with
654 siRNA using Lipofectamine RNAiMax (Thermo Fisher Scientific). For each well to be trans-
655 fected, was first prepared the RNAi duplex-Lipofectamine RNAiMAX complexes as follows:
656 6 pmol of RNAi duplex were diluted in 100 µl Opti-MEM I Medium without serum in the well
657 of the culture plate and gently mixed. Then, 1 µl Lipofectamine RNAiMAX was added to
658 each well containing the diluted RNAi molecules, gently mixed and incubated for 20
659 minutes at room temperature under sterile conditions. In that time cells were detached,
660 counted, and diluted in complete growth medium without antibiotics so that 500 µl contains
661 the appropriate number of cells to give 30% confluence 24 hours after plating. After the 20

662 minutes of incubation at room temperature to each well with RNAi duplex - Lipofectamine
663 RNAiMAX complexes were added 500 µl of the diluted cells. This gives a final volume of
664 600 µl and a final RNA concentration of 10 nM. The 24well-plate was gently mixed gently
665 by rocking and incubated 24-72 hours at 37°C in a CO2 incubator.
666 The siRNA targeting VPS35 was from Sigma (5' CTGGACATATTTATCAATATA 3'; 3' TA-
667 TATTGATAAATATGTCCAG 5'). It was used at 10 nM final concentration. Control cells
668 were treated with identical concentrations of siGENOME Control Pool Non-Targeting from
669 Dharmacon (D-001206-13-05).
670
671 *Immunostaining*
672 HK2 cells were grown to 70% confluence on glass coverslips before immunofluorescence
673 microscopy was performed. Cells were fixed for 10 min in 4% paraformaldehyde in PBS
674 (phosphate-buffered saline). After fixation, cells were incubated (30 min at room tempera-
675 ture) in blocking buffer with (permeabilized cells) or without (non-permeabilized cells)
676 0.05% (w:v) saponin (Sigma-Aldrich, 558255), 0.5% (w:v) BSA and 50 mM NH_4Cl in PBS.
677 The cells were incubated for 1 h with primary antibody in blocking buffer, washed three
678 times in PB and incubated for 1 h with the secondary antibody in blocking buffer. Then,
679 cells were washed three times in PBS, mounted with Mowiol (Sigma-Aldrich, 475904-M)
680 on slides and analysed by confocal microscopy.
681 Primary antibodies were anti-LAMP1 (H4A3, USBiologicvak Life Sciences) and anti-Glut1
682 (ab15309 Abcam). Secondary antibodies were Cy3-conjugated AffiniPure Donkey anti-
683 Mouse IgG H+L (Jackson Immuno Research); Cy3-conjugated AffiniPure Donkey anti-
684 Rabbit IgG H+L (Jackson Immuno Research); Alexa fluor®488-conjugated AffiniPure Don-
685 key anti-Rabbit IgG H+L (Jackson Immuno Research).
686
687 *Confocal fluorescence microscopy and image processing.*
688 Confocal microscopy was performed on an inverted confocal laser microscope (Zeiss LSM
689 880 with airyscan) with a 63x 1.4 NA oil immersion lens. Z-stack Images were acquired on
690 a Zeiss LSM880 microscope with Airyscan. GLUT1-fluorescence was quantified using Im-
691 ageJ. Individual cells were selected using the freeform drawing tool to create a ROI (ROI).
692 The 'Measure' function provided the area, the mean grey value and integrated intensity of
693 the ROI. The mean background level was obtained by measuring the intensity in three dif-
694 ferent regions outside the cells, dividing them by the area of the regions measured, and

695 averaging the values obtained. This background noise was removed from each cell, yield-
696 ing the CTCF (corrected total cell fluorescence): CTCF=integrated intensity of cell ROI −
697 (area of ROI × mean fluorescence of background).
698 To quantify the degree of co-localisation, confocal z-stacks were acquired. Single chan-
699 nels from each image in 8-bit format were thresholded to subtract background and then
700 the "Just Another Colocalisation Plug-in" (JACOP) of ImageJ was used to measure the
701 Pearson's correlation coefficient.
702
703 **Gel electrophoresis and Western blot**
704 Ctrl and Vps35-KD HK2 cells were plated into 12-well tissue culture test plates (TPP) until
705 72h after transfection with the siRNAs. Cells were then washed three times with ice-cold
706 PBS, scraped, and proteins were extracted in ice-cold lysis buffer (150 mM NaCl, 2 mM
707 EDTA, 40 mM HEPES, and 1% Triton X-100) supplemented with phosphatase (Roche
708 #04906837001) and protease inhibitor cocktail. Protease inhibitor (PI) cocktail (final con-
709 centrations: 40 µM pefablock SC (Merck, 11,429,876,001), 2.1 µM leupeptin (Merck,
710 11,529,048,001), 80 µM o-phenantroline (Merck,131,377), 1.5 µM pepstatin A (Merck,
711 11,524,488,001). Protein extracts were supplemented with 1/4 volume of 5x reducing sam-
712 ple buffer (250 mM Tris-Cl, pH 6.8, 5% β-mercaptoethanol, 10% SDS, 30% glycerol,
713 0.02% bromophenol blue) and heated to 95 °C for 5 min. The samples were run on SDS-
714 polyacrylamide gels (W x L x H: 8.6 x 6.8 x 0.15 cm). Running gels were either 8% or 4-
715 16% protogel (30% w/v acrylamide, 0.8% bisacrylamide (37.5:1 solution, National diagnos-
716 tics, Atlanta, USA),, 0.38 M Tris, pH 8.8, 0.1% w/v SDS (Applichem, 475904-M), 0.06%
717 TEMED (Applichem, A1148), 0.06% w/v APS (Applichem, A2941). The stacking gels were
718 prepared as follows: 6% acrylamide, 0.16% bis-acrylamide, 0.1 M Tris, pH 6.8, 0.1% SDS,
719 0.1% TEMED, 0.05% ammonium persulfate. The gels were run at constant current (35
720 mA). Proteins were blotted onto 0.45 µm nitrocellulose membrane (Amersham) overnight
721 at a constant current of 200 mA using a Trans-Blot® Cell (Bio-Rad, USA).
722 After incubation with the primary antibody, signals were detected by secondary antibodies
723 coupled to infrared dyes (LI-COR) and detected on a LI-COR Odyssey Infrared Imager.
724 Images were exported as TIFF files and processed in Adobe Photoshop. Band intensity
725 was quantified using ImageJ band analysis (Schneider CA et al., 2012). We used anti-
726 LAMP1 (H4A3, USBiologicvak Life Sciences), anti-Tubulin (T9026 Sigma-Aldrich) anti-
727 Vps35 (ab10099 Abcam, ab157220 Abcam).
728

729 **Statistics**

730 Where averages were calculated, the values stem from experiments that were performed
731 independently. For all experiments, significance of differences was tested by a two-tailed t-
732 test.

733

734

735 **Acknowledgements**

736 We thank Christian Ungermann for strains expressing CSC and SNX. This work was sup-
737 ported by grants from the SNSF (179306 and 204713) and ERC (788442) to AM.

738

References

Angelova MI, Soléau S, Méléard Ph, Faucon F & Bothorel P (1992) Trends in Colloid and Interface Science VI. *Prog Colloid Polym Sci*: 127–131

Balderhaar HJK, Arlt H, Ostrowicz C, Bröcker C, Sündermann F, Brandt R, Babst M & Ungermann C (2010) The Rab GTPase Ypt7 is linked to retromer-mediated receptor recycling and fusion at the yeast late endosome. *J Cell Sci* 123: 4085–4094

Burda P, Padilla SM, Sarkar S & Emr SD (2002) Retromer function in endosome-to-Golgi retrograde transport is regulated by the yeast Vps34 PtdIns 3-kinase. *J Cell Sci* 115: 3889–3900

Cameron LA, Footer MJ, Oudenaarden A van & Theriot JA (1999) Motility of ActA protein-coated microspheres driven by actin polymerization. *PNAS* 96: 4908–4913

Chadwick SR, Grinstein S & Freeman SA (2021) From the inside out: Ion fluxes at the centre of endocytic traffic. *Curr Opin Cell Biol* 71: 77–86

Cheever ML, Sato TK, Beer T de, Kutateladze TG, Emr SD & Overduin M (2001) Phox domain interaction with PtdIns(3)P targets the Vam7 t-SNARE to vacuole membranes. *Nat Cell Biol* 3: 613–618

Chen K-E, Healy MD & Collins BM (2019) Towards a molecular understanding of endosomal trafficking by Retromer and Retriever. *Traffic*: tra.12649

Chi RJ, Liu J, West M, Wang J, Odorizzi G & Burd CG (2014) Fission of SNX-BAR-coated endosomal retrograde transport carriers is promoted by the dynamin-related protein Vps1. *J Cell Biol* 204: 793–806

Chiaruttini N, Redondo-Morata L, Colom A, Humbert F, Lenz M, Scheuring S & Roux A (2015) Relaxation of Loaded ESCRT-III Spiral Springs Drives Membrane Deformation. *Cell* 163: 866–879

Collins BM, Norwood SJ, Kerr MC, Mahony D, Seaman MNJ, Teasdale RD & Owen DJ (2008) Structure of Vps26B and mapping of its interaction with the retromer protein complex. *Traffic* 9: 366–379

Collins BM, Skinner CF, Watson PJ, Seaman MNJ & Owen DJ (2005) Vps29 has a phosphoesterase fold that acts as a protein interaction scaffold for retromer assembly. *Nat Struct Mol Biol* 12: 594–602

Colom A, Redondo-Morata L, Chiaruttini N, Roux A & Scheuring S (2017) Dynamic remodeling of the dynamin helix during membrane constriction. *Proc National Acad Sci* 114: 5449–5454

774 Courtellemont T, Leo MGD, Gopaldass N & Mayer A (2022) CROP: a retromer-PROPPIN
775 complex mediating membrane fission in the endo-lysosomal system. *Embo J* 41:
776 e109646

777 Cui Y, Carosi JM, Yang Z, Ariotti N, Kerr MC, Parton RG, Sargeant TJ & Teasdale RD
778 (2018) Retromer has a selective function in cargo sorting via endosome transport carri-
779 ers. *J Cell Biol*: jcb.201806153

780 Dar S, Kamerkar SC & Pucadyil TJ (2015) A high-throughput platform for real-time analy-
781 sis of membrane fission reactions reveals dynamin function. *Nat Cell Biol*

782 Daumke O, Lundmark R, Vallis Y, Martens S, Butler PJG & McMahon HT (2007) Architec-
783 tural and mechanistic insights into an EHD ATPase involved in membrane remodelling.
784 *Nature* 449: 923–927

785 Deatherage CL, Nikolaus J, Karatekin E & Burd CG (2020) Retromer forms low order oli-
786 gomers on supported lipid bilayers. *J Biol Chem*: jbc.RA120.013672

787 DeLeo MG, Berger P & Mayer A (2021) WIPI1 promotes fission of endosomal transport
788 carriers and formation of autophagosomes through distinct mechanisms. *Autophagy*: 1–
789 27

790 Derivery E, Sousa C, Gautier JJ, Lombard B, Loew D & Gautreau A (2009) The Arp2/3 ac-
791 tivator WASH controls the fission of endosomes through a large multiprotein complex.
792 *Dev Cell* 17: 712–723

793 Desfougères Y, Neumann H & Mayer A (2016) Organelle size control - increasing vacuole
794 content activates SNAREs to augment organelle volume through homotypic fusion. *J*
795 *Cell Sci* 129: 2817–2828

796 Evans AJ, Daly JL, Anuar ANK, Simonetti B & Cullen PJ (2020) Acute inactivation of retro-
797 mer and ESCPE-1 leads to time-resolved defects in endosomal cargo sorting. *J Cell Sci*
798 133: jcs246033

799 Gierke S, Kumar P & Wittmann T (2010) Analysis of microtubule polymerization dynamics
800 in live cells. *Methods Cell Biol* 97: 15–33

801 Gokool S, Tattersall D & Seaman MNJ (2007) EHD1 interacts with retromer to stabilize
802 SNX1 tubules and facilitate endosome-to-Golgi retrieval. *Traffic* 8: 1873–1886

803 Gomez TS & Billadeau DD (2009) A FAM21-containing WASH complex regulates retro-
804 mer-dependent sorting. *Dev Cell* 17: 699–711

805 Goode BL, Eskin JA & Wendland B (2015) Actin and Endocytosis in Budding Yeast. *Ge-*
806 *netics* 199: 315–358

807 Gopaldass N, Fauvet B, Lashuel H, Roux A & Mayer A (2017) Membrane scission driven
808 by the PROPPIN Atg18. *EMBO J* 36: 3274–3291

809 Güldener U, Heck S, Fiedler T, Beinhauer J & Hegemann JH (1996) A new efficient gene
810 disruption cassette for repeated use in budding yeast. *Nucleic Acids Res* 24: 2519–
811 2524

812 Harbour ME, Breusegem SY & Seaman MNJ (2012) Recruitment of the endosomal WASH
813 complex is mediated by the extended "tail" of Fam21 binding to the retromer protein
814 Vps35. *Biochem J* 442: 209–220

815 Harrison MS, Hung C-S, Liu T, Christiano R, Walther TC & Burd CG (2014) A mechanism
816 for retromer endosomal coat complex assembly with cargo. *Proc Natl Acad Sci USA*
817 111: 267–272

818 Harterink M, Port F, Lorenowicz MJ, McGough IJ, Silhankova M, Betist MC, Weering JRT
819 van, Heesbeen RGHP van, Middelkoop TC, Basler K, *et al* (2011) A SNX3-dependent
820 retromer pathway mediates retrograde transport of the Wnt sorting receptor Wntless
821 and is required for Wnt secretion. *Nat Cell Biol* 13: 914–923

822 Hesketh GG, Pérez-Dorado I, Jackson LP, Wartosch L, Schäfer IB, Gray SR, McCoy AJ,
823 Zeldin OB, Garman EF, Harbour ME, *et al* (2014) VARP Is Recruited on to Endosomes
824 by Direct Interaction with Retromer, Where Together They Function in Export to the Cell
825 Surface. *Dev Cell* 29: 591–606

826 Hierro A, Rojas AL, Rojas R, Murthy N, Effantin G, Kajava AV, Steven AC, Bonifacino JS
827 & Hurley JH (2007) Functional architecture of the retromer cargo-recognition complex.
828 *Nature* 449: 1063–1067

829 Horazdovsky BF, Davies BA, Seaman MN, McLaughlin SA, Yoon S & Emr SD (1997) A
830 sorting nexin-1 homologue, Vps5p, forms a complex with Vps17p and is required for re-
831 cycling the vacuolar protein-sorting receptor. *Mol Biol Cell* 8: 1529–1541

832 Hsieh W-T, Hsu C-J, Capraro BR, Wu T, Chen C-M, Yang S & Baumgart T (2012) Curva-
833 ture sorting of peripheral proteins on solid-supported wavy membranes. *Langmuir : the*
834 *ACS journal of surfaces and colloids* 28: 12838–12843

835 Janke C, Magiera MM, Rathfelder N, Taxis C, Reber S, Maekawa H, Moreno-Borchart A,
836 Doenges G, Schwob E, Schiebel E, *et al* (2004) A versatile toolbox for PCR-based tag-
837 ging of yeast genes: new fluorescent proteins, more markers and promoter substitution
838 cassettes. *Yeast* 21: 947–962

839 Jia D, Gomez TS, Billadeau DD & Rosen MK (2012) Multiple repeat elements within the
840 FAM21 tail link the WASH actin regulatory complex to the retromer. *Mol Biol Cell* 23:
841 2352–2361

842 Jia D, Zhang J-S, Li F, Wang J, Deng Z, White MA, Osborne DG, Phillips-Krawczak C,
843 Gomez TS, Li H, *et al* (2016) Structural and mechanistic insights into regulation of the
844 retromer coat by TBC1d5. *Nature communications* 7: 1–11

845 Jung H, Robison AD & Cremer PS (2009) Detecting protein-ligand binding on supported
846 bilayers by local pH modulation. *J Am Chem Soc* 131: 1006–1014

847 Kaksonen M (2008) Taking apart the endocytic machinery. *J Cell Biol* 180: 1059–1060

848 Kendall AK, Chandra M, Xie B, Wan W & Jackson LP (2022) Improved mammalian retro-
849 mer cryo-EM structures reveal a new assembly interface. *Biorxiv*: 2022.03.04.482375

850 Kendall AK, Xie B, Xu P, Wang J, Burcham R, Frazier MN, Binshtein E, Wei H, Graham
851 TR, Nakagawa T, *et al* (2020) Mammalian Retromer Is an Adaptable Scaffold for Cargo
852 Sorting from Endosomes. *Structure* 28: 393-405.e4

853 Kovtun O, Leneva N, Bykov YS, Ariotti N, Teasdale RD, Schaffer M, Engel BD, Owen DJ,
854 Briggs JAG & Collins BM (2018) Structure of the membrane-assembled retromer coat
855 determined by cryo-electron tomography. *Nature* 561: 561–564

856 Kukulski W, Schorb M, Welsch S, Picco A, Kaksonen M & Briggs JAG (2012) Chapter 13
857 Precise, Correlated Fluorescence Microscopy and Electron Tomography of Lowicryl
858 Sections Using Fluorescent Fiducial Markers. *Methods Cell Biol* 111: 235–257

859 Kvainickas A, Jimenez-Orgaz A, Nägele H, Hu Z, Dengjel J & Steinberg F (2017) Cargo-
860 selective SNX-BAR proteins mediate retromer trimer independent retrograde transport.
861 *J Cell Biology* 216: 3677–3693

862 Leneva N, Kovtun O, Morado DR, Briggs JAG & Owen DJ (2021) Architecture and mecha-
863 nism of metazoan retromer:SNX3 tubular coat assembly. *Sci Adv* 7: eabf8598

864 Liu T, Gomez TS, Sackey BK, Billadeau DD & Burd CG (2012) Rab GTPase regulation of
865 retromer-mediated cargo export during endosome maturation. *Mol Biol Cell* 23: 2505–
866 2515

867 Lucas M, Gershlick DC, Vidaurrazaga A, Rojas AL, Bonifacino JS & Hierro A (2016) Struc-
868 tural Mechanism for Cargo Recognition by the Retromer Complex. *Cell* 167: 1623-
869 1635.e14

870 Luzio JP, Hackmann Y, Dieckmann NMG & Griffiths GM (2014) The biogenesis of lyso-
871 somes and lysosome-related organelles. *Cold Spring Harb Perspect Biol* 6: a016840–
872 a016840

873 Marcusson EG, Horazdovsky BF, Cereghino JL, Gharakhanian E & Emr SD (1994) The
874 sorting receptor for yeast vacuolar carboxypeptidase Y is encoded by the VPS10 gene.
875 *Cell* 77: 579–586

876 Marquardt L, Taylor M, Kramer F, Schmitt K, Braus GH, Valerius O & Thumm M (2022)
877 Vacuole fragmentation depends on a novel Atg18-containing retromer-complex. *Au-*
878 *tophagy*: 1–18

879 Muriel O, Michon L, Kukulski W & Martin SG (2021) Ultrastructural plasma membrane
880 asymmetries in tension and curvature promote yeast cell fusion. *J Cell Biol* 220:
881 e202103142

882 Nothwehr SF, Bruinsma P & Strawn LA (1999) Distinct Domains within Vps35p Mediate
883 the Retrieval of Two Different Cargo Proteins from the Yeast Prevacuolar/Endosomal
884 Compartment. *Mol Biol Cell* 10: 875–890

885 Peters C, Baars TL, Buhler S & Mayer A (2004) Mutual control of membrane fission and
886 fusion proteins. *Cell* 119: 667–678

887 Phillips-Krawczak CA, Singla A, Starokadomskyy P, Deng Z, Osborne DG, Li H, Dick CJ,
888 Gomez TS, Koenecke M, Zhang J-S, *et al* (2015) COMMD1 is linked to the WASH com-
889 plex and regulates endosomal trafficking of the copper transporter ATP7A. *Mol Biol Cell*
890 26: 91–103

891 Purushothaman LK, Arlt H, Kuhlee A, Raunser S & Ungermann C (2017) Retromer-driven
892 membrane tubulation separates endosomal recycling from Rab7/Ypt7-dependent fu-
893 sion. *Mol Biol Cell* 28: 783–791

894 Purushothaman LK & Ungermann C (2018) Cargo induces retromer-mediated membrane
895 remodeling on membranes. *Mol Biol Cell* 29: 2709–2719

896 Rojas R, Kametaka S, Haft CR & Bonifacino JS (2007) Interchangeable but essential func-
897 tions of SNX1 and SNX2 in the association of retromer with endosomes and the traffick-
898 ing of mannose 6-phosphate receptors. *Mol Cell Biol* 27: 1112–1124

899 Rojas R, Vlijmen T van, Mardones GA, Prabhu Y, Rojas AL, Mohammed S, Heck AJR,
900 Raposo G, Sluijs P van der & Bonifacino JS (2008) Regulation of retromer recruitment
901 to endosomes by sequential action of Rab5 and Rab7. *J Cell Biol* 183: 513–526

902 Roux A (2013) The physics of membrane tubes: soft templates for studying cellular mem-
903 branes. *Soft Matter* 9: 6726–6736

904 Roux A, Koster G, Lenz M, Sorre B, Manneville J-B, Nassoy P & Bassereau P (2010)
905 Membrane curvature controls dynamin polymerization. *Proc National Acad Sci* 107:
906 4141–4146

907 Saric A & Freeman SA (2020) Endomembrane Tension and Trafficking. *Front Cell Dev*
908 *Biol* 8: 611326

909 Scott CC, Vacca F & Gruenberg J (2014) Endosome maturation, transport and functions.
910 *Semin Cell Dev Biol* 31: 2–10

911 Seaman MN, McCaffery JM & Emr SD (1998) A membrane coat complex essential for en-
912 dosome-to-Golgi retrograde transport in yeast. *J Cell Biol* 142: 665–681

913 Seaman MNJ, Harbour ME, Tattersall D, Read E & Bright N (2009) Membrane recruitment
914 of the cargo-selective retromer subcomplex is catalysed by the small GTPase Rab7 and
915 inhibited by the Rab-GAP TBC1D5. *J Cell Sci* 122: 2371–2382

916 Seaman MNJ & Williams HP (2002) Identification of the functional domains of yeast sort-
917 ing nexins Vps5p and Vps17p. *Mol Biol Cell* 13: 2826–2840

918 Sheff MA & Thorn KS (2004) Optimized cassettes for fluorescent protein tagging in Sac-
919 charomyces cerevisiae. *Yeast* 21: 661–670

920 Simonetti B, Guo Q, Giménez-Andrés M, Chen K-E, Moody ERR, Evans AJ, Chandra M,
921 Danson CM, Williams TA, Collins BM, *et al* (2022) SNX27–Retromer directly binds

ESCPE-1 to transfer cargo proteins during endosomal recycling. *Plos Biol* 20: e3001601

Simonetti B, Paul B, Chaudhari K, Weeratunga S, Steinberg F, Gorla M, Heesom KJ, Bashaw GJ, Collins BM & Cullen PJ (2019) Molecular identification of a BAR domain-containing coat complex for endosomal recycling of transmembrane proteins. *Nat Cell Biol* 21: 1219–1233

Simunovic M, Manneville J-B, Renard H-F, Evergren E, Raghunathan K, Bhatia D, Kenworthy AK, Voth GA, Prost J, McMahon HT, *et al* (2017) Friction Mediates Scission of Tubular Membranes Scaffolded by BAR Proteins. *Cell* 170: 172-184.e11

Solinger JA, Rashid H-O, Prescianotto-Baschong C & Spang A (2020) FERARI is required for Rab11-dependent endocytic recycling. *Nat Cell Biol* 59: 237–12

Song X, Xu W, Zhang A, Huang G, Liang X, Virbasius JV, Czech MP & Zhou GW (2001) Phox homology domains specifically bind phosphatidylinositol phosphates. *Biochemistry* 40: 8940–8944

Steinberg F, Gallon M, Winfield M, Thomas EC, Bell AJ, Heesom KJ, Tavaré JM & Cullen PJ (2013) A global analysis of SNX27–retromer assembly and cargo specificity reveals a function in glucose and metal ion transport. *Nat Cell Biol* 15: 461–471

Strochlic TI, Setty TG, Sitaram A & Burd CG (2007) Grd19/Snx3p functions as a cargo-specific adapter for retromer-dependent endocytic recycling. *J Cell Biology* 177: 115–125

Temkin P, Lauffer B, Jäger S, Cimermancic P, Krogan NJ & Zastrow M von (2011) SNX27 mediates retromer tubule entry and endosome-to-plasma membrane trafficking of signalling receptors. *Nat Cell Biol* 13: 715–721

Weering JRT van, Sessions RB, Traer CJ, Kloer DP, Bhatia VK, Stamou D, Carlsson SR, Hurley JH & Cullen PJ (2012) Molecular basis for SNX-BAR-mediated assembly of distinct endosomal sorting tubules. *EMBO J* 31: 4466–4480

Yu JW & Lemmon MA (2001) All phox homology (PX) domains from Saccharomyces cerevisiae specifically recognize phosphatidylinositol 3-phosphate. *Journal of Biological Chemistry* 276: 44179–44184

Zhang Y, Pang X, Li J, Xu J, Hsu VW & Sun F (2021) Structural insights into membrane remodeling by SNX1. *Proc Natl Acad Sci USA* 118

Zieger M & Mayer A (2012) Yeast vacuoles fragment in an asymmetrical two-phase process with distinct protein requirements. *Mol Biol Cell* 23: 3438–3449

958 **Figure legends**

959

960 **Figure 1: Assembly of retromer coats on supported membrane tubes.**

961 **a**. Dynamics of scaffold formation. 25 nM SNX and 25 nM $CSC^{mClover}$ in PBS was added to
962 SMTs and imaged by confocal microscopy at a frame rate of 1 Hz for 5 min.

963 **b**. Kymograph of the tubule shown in a. See movie 1.

964 **c**. SNX^{GFP} colocalizes with CSC^{mRuby} on SMTs. SMTs containing 1mol % of the fluorescent
965 lipid Cy5.5-PE were incubated with 25 nM of SNX^{GFP} and CSC^{mRuby} for 2 min. Then, the
966 tubes were imaged by confocal microscopy.

967 **d**. Line scan analysis along the boxed tubule from c.

968 **e**. Scaffold formation at low SNX concentration is facilitated by CSC. SMTs were incubated
969 as in a, using 10 nM SNX^{GFP} in combination with either 50 nM CSC or only control buffer.

970 **f**. Scaffold formation by elevated concentrations of SNX alone. 100 nM SNX-GFP was
971 added to SMTs and imaged by confocal microscopy at a rate of 0.5 Hz for 5 min.

972 **g**. Kymograph of the tubule highlighted in f. **h.** line scan analysis of the tubule highlighted
973 in f. This experiment is also shown in movie 2.

974

975

976 **Figure 2. Constriction of membrane tubes by SNX and SNX/CSC**

977 **a**. SMTs labelled with Texas-Red DHPE were incubated with non-tagged proteins at 25°C
978 for 3 to 5 min and analyzed by fluorescence microscopy. Proteins were used at the follow-
979 ing concentrations: 100 nM SNX; 25 nM SNX/25 nM CSC; 50 nM dynamin.

980 **b.** Line scan analysis along the tubules from a. The lower boundaries of fluorescence are
981 indicated by horizontal lines in the respective colors**.**

982 **c**. Distribution of Texas-Red DHPE fluorescence in constricted domains for tubules coated
983 by SNX (n = 16), SNX+CSC (n = 18), or dynamin (n = 15). ****: $p < 0.0001$

984 **d.** Constricted domain radius as a function of starting (non-constricted) tube radius. Radii
985 of constricted and non-constricted regions of a variety of lipid tubes were determined using
986 the known diameter of a dynamin-coated tube as a reference. Experiments were per-
987 formed as in a, using 25 nM SNXs (n = 16) or 25 nM SNX plus 25 nM CSC (n = 18).

988 **e**. Binding of $CSC^{mClover}$ to constricted SNX domains. SMTs were first incubated with 100
989 nM SNX for 2 min at 25°C until constriction zones were visible through reduced lipid fluo-
990 rescence. Then, 50 nM $CSC^{mClover}$ was added under continuous acquisition at 0.5 Hz.

991 **f**. Kymograph of a tubule from e.

992 **g**. Quantification of Texas-Red-DHPE fluorescence under the constriction zone before and
993 after $CSC^{mClover}$ addition (n = 16). Error bars represent the standard deviation from the
994 mean. n.s.: not significant (p=0.235).
995
996 **Fig. 3: Bidirectional elongation of the coat**
997 **a.** Scheme of the experiment
998 **b**. SMTs labelled with Cy5.5-PE were first incubated with 50 nM SNX and 50 nM CSC^{mRuby}
999 at 25°C until coat formation was initiated (~90 sec). Then, non-bound SNX and CSC^{mRuby}
1000 were washed out and the tubes were subjected to a second incubation with 50 nM SNX
1001 and 50 nM $CSC^{mClover}$ (3 min). Tubes were imaged by confocal microscopy at a framerate
1002 of 0.5 Hz. **c**. Kymograph of the tubule shown in b.
1003
1004 **Fig. 4: Stabilization of pulled membrane tubes by CSC/SNX.**
1005 **a.** Coat formation on a pulled membrane tubule. Confocal pictures of a GUV labelled with
1006 Rhodamine-DHPE (red). A membrane tubule has been pulled from the GUV through a
1007 small bead and optical tweezers. The GUV is shown before and at several time points af-
1008 ter ejection of SNX/$CSC^{mClover}$ (green) from a pipette in the vicinity of the GUV.
1009 **b.** Measurement of the force exerted on the bead as a function of time after protein ejec-
1010 tion, taken from the experiment in a.
1011 **c.** Repetitive pulling and stabilization. Confocal pictures of a GUV labelled with Rhoda-
1012 mine-DHPE (red). A tubule has been pulled as in a and SNX/$CSC^{mClover}$ (green) was
1013 added. The GUV is shown before and after protein ejection, and at several stages of sub-
1014 sequent re-pulling and stabilization through additional coat recruitment. Protein quickly
1015 populates new tube regions generated by pulling back the GUV.
1016 **d**. Measurement of the force exerted on the bead as a function of time for the experiment
1017 shown in c. Arrowheads mark the timepoints when the GUV has been pulled back.
1018 **e**. Kymograph of the portion of the tubule boxed in d, showing growth of retromer coat into
1019 a newly pulled portion of the tubule.
1020
1021 **Figure 5: Variable saturation of the SNX layer with CSC**
1022 **a.** Recruitment of additional subunits to pre-formed coats using differentially labelled CSC
1023 and SNX. Scheme of the experiment shown in b and c.
1024 **b**. Coats were formed on SMTs using 25 nM SNX and 25 nm CSC^{mRuby}. Excess protein
1025 was washed out with buffer and 50 nM SNX^{GFP} or 50 nM $CSC^{mClover}$ were added. SMTs

1026 were imaged after SNX/CSC^{mRuby} coat formation and 2 min after addition of CSC^{mClover} or
1027 SNX^{GFP}.
1028 **c**. Ratio of CSC^{mRuby} signals in the constricted areas before and after addition of CSC^{mClo-}
1029 ^{ver}.
1030 **d**. Occupation of SNX domains with CSC as a function of the starting radius of the tube
1031 (naked tube radius). Arrays of SMTs were incubated with 25 nM SNX and 25 nM CSC^{mClo-}
1032 ^{ver}. The density of CSC^{mClover} in constricted domains was traced through its fluorescence
1033 signal. The starting radius of the tube was estimated through Texas Red-DHPE fluores-
1034 cence in non-constricted regions and calibration with dynamin. This radius is indicated for
1035 each tube.
1036 **e**. The density of CSC^{mClover} in SNX/CSC^{mClover} coats from d was plotted as a function of
1037 the radius of the non-constricted tube.
1038 **f**. Experiment as in d using 25 nM SNX^{GFP} and 25 nM CSC.
1039 **g**. The fluorescence signals of SNX^{GFP} in SNX/CSC coats from f were quantified plotted as
1040 a function of the radius of the non-constricted tube as in e.
1041
1042 **Figure 6. Substitutions destabilizing the Vps35-Vps35 interface.**
1043 **a.** Structure of the pentameric retromer complex (Leneva *et al*, 2021). The boxes highlight
1044 the Vps35 dimerization interface. Residues substituted in *vps35^{PISA}* and *vps35^{AAA3KE}* are
1045 shown red and green, respectively, in the structure from C. thermophilum and in a model
1046 of the S. cerevisiae complex derived from the Chaetomium thermophilum structure (PDB
1047 7BLR using the online modelling tool Swiss-model (https://swissmodel.expasy.org).
1048 **b**. Sequence alignment of the Vps35 dimerization domains from different species. Amino
1049 acids substituted in *vps35^{PISA}* and *vps35^{AAA3KE}* are shown in red and green, respectively.
1050 One residue (in red-green) is shared between the two.
1051 **c.** Coomassie-stained SDS-PAGE gel of purified CSC^{mClover} complexes containing the indi-
1052 cated Vps35 variants.
1053 **d**. Blue native PAGE gel showing the formation of higher order assemblies for CSC^{mClover}
1054 complexes containing Vps35 variants and their tentative assignment as monomers, dimers
1055 and tetramers.
1056
1057 **Figure 7: Effect of Vps35 dimerization on coat constriction**
1058 **a**. Experimental setup: SMTs labelled with Texas Red DHPE were preincubated with 25
1059 nM SNX for 3 min to load them with SNX but not allow formation of constrictions. After a

1060 wash with protein-free buffer, 50 nM of $CSC^{mClover}$ carrying the indicated Vps35 variants
1061 was added. The tubes were imaged by confocal microscopy at a framerate of 0.5 Hz.
1062 **b** Images of three timepoints after addition of $CSC^{mClover}$ variants.
1063 **c** Kymographs of the entire reactions. Experiments are shown in movies 3-5.
1064 **d**. Recruitment kinetics of $CSC^{mClover}$ variants to SNX-decorated SMTs during the second
1065 incubation phase. mClover fluorescence appearing along the entire length of the tubes
1066 was quantified over time. n=10 tubes per variant. Curves represent the mean and shaded
1067 areas around the curves represent the SEM.
1068
1069 **Figure 8: In vivo effect of Vps35 dimerization mutants on Vps10 in yeast**
1070 **a**. $Vps10^{yEGFP}$ localization. Yeast cells carrying $Vps10^{yEGFP}$ and expressing the indicated
1071 vps35 alleles as the sole source of Vps35 were logarithmically grown in SC medium. Their
1072 vacuoles were labelled with FM4-64. Cells were harvested by brief centrifugation and im-
1073 mediately imaged by confocal microscopy. Single confocal planes are shown. A brightfield
1074 image was used to outline the cell boundaries (shown in the merged images). Scale bar: 5
1075 µM.
1076 **b**. Co-localization of $Vps10^{yEGFP}$ and FM4-64 in cells from a was measured using Pear-
1077 son's coefficient.
1078 **c**. CLEM analysis of $Vps10^{yEGFP}$ localization in $vps35^{PISA}$ mutant cells. Logarithmically
1079 growing cells were high-pressure frozen and processed by freeze substitution and embed-
1080 ding.
1081
1082 **Fig. 9: Effects of Vps35 dimerization mutants in human kidney (HK2) cells**
1083 **a**. GLUT1 at the plasma membrane. HK2 cells were treated with siRNA targeting VPS35
1084 or with mock siRNA. Cells were fixed and stained with antibody to GLUT1 (red) and with
1085 DAPI (blue). Cells were not detergent permeabilized in order to preferentially show GLUT1
1086 at the cell surface. Maximum projections of image stacks (step size in z of 300 nm) are
1087 shown. Scale bars: 10 µm.
1088 **b**. Influence of VPS35 variants on GLUT1. HK2 cells silenced for VPS35 were transfected
1089 with a plasmid carrying siRNA resistant wildtype or mutant forms of GFP-VPS35. GLUT1
1090 was detected by fixation and immunofluorescence staining as in a. Maximum projections
1091 of image stacks (step size in z of 300 nm) are shown. Scale bars: 10 µm.
1092 **c**. Quantification of GLUT1 immunofluorescence in cells from (b). Regions of interest
1093 (ROIs) corresponding to cells expressing the indicated VPS35 variants, and some regions

1094 outside the cells (background), were manually defined using ImageJ software. Total cell
1095 fluorescence was integrated and corrected for background fluorescence. 105 cells per
1096 condition stemming from 3 independent experiments were analyzed. P values were calcu-
1097 lated by Welch's t-test. The analysis was performed with 99% confidence: *** $p < 0.001$.
1098 **d.** Expression of Vps35 variants in cells from b was analyzed by SDS-PAGE and Western
1099 blot against Vps35. Tubulin served as loading control.
1100 **e.** Quantification of the Vps35/tubulin ratio in cells from b. Data stems from three inde-
1101 pendent experiments and show the mean. NS: not significant ($p>0.01$).
1102
1103
1104

1105 **Supplementary Figures**

1106

1107 **Suppl. Figure 1: SNX and CSC proteins extracted from yeast**

1108 The indicated TAP-tagged protein complexes were extracted from yeast and analyzed by
1109 SDS-PAGE and Coomassie staining.

1110

1111 **Suppl. Figure 2: Lipid and SNX dependence of CSC binding and constriction of tu-**
1112 **bules**

1113 **a.** PI3P and SNX dependence of CSC recruitment. SMTs were prepared with or without
1114 PI3P, incubated with 25 nM $CSC^{mClover}$ in the presence or absence of 25 nM SNX complex
1115 and analyzed by fluorescence microscopy. Scale bars: 2 µm.

1116 **b**. Coat formation and tube constriction shown through NBD-PC, a lipid labelled at a fatty
1117 acyl chain. SMTs labelled with NBD-PC instead of Cy5.5-PE were incubated with SNX and
1118 $CSC^{mClover}$ as in Fig. 1a and analyzed by fluorescence microscopy.

1119 **c.** Line scan analysis of the tubule shown in b.

1120

1121 **Suppl. Figure 3: Procedure for quantifying constrictions along tubules**

1122 A series of line scans were performed along the entire length of an SMT, perpendicular to
1123 the tube. For each line scan, a Gaussian curve was fitted, and the maximum height of the
1124 coat signal (e.g. GFP) and the lipid signal (e.g. Texas Red DHPE) were extracted. The
1125 maximum height was then plotted against the intensity of the lipid signal along the same
1126 scan. This was performed for every line scan along the tube, yielding two populations. The
1127 number of dots in each population are a measure for the length of constricted and non-
1128 constricted regions. For each tube, the zones corresponding to the constricted and non-
1129 constricted areas were determined manually and their mean fluorescence value was used
1130 to calculate the tube diameter by comparison with the signals obtained with dynamin-
1131 coated tubes.

1132

1133 **Suppl. Figure 4**: **Lack of constricted domain formation after co-incubating SNX with**
1134 **CSC containing *vps35^{PISA}* or *vps35^{AAA3KE}*.**

1135 **a, b.** SMT assay with the dimerization mutants. 50 nM SNX and 50 nM of $CSC^{mClover}$ carry-
1136 ing the indicated Vps35 variants were incubated with SMTs and imaged by confocal mi-
1137 croscopy. Scale bars: 2 µm

1138 **c**. Binding of CSC variants to preformed SNX domains. SMTs were incubated with high
1139 SNX concentration (100 nM) for 2 min to pre-form constrictions zones. Unbound SNX was
1140 washed away and 50 nM $CSC^{mClover}$ containing the indicated Vps35 variants was added.
1141 Panels show tubes before SNX addition (0 sec), after the formation of SNX only coats (192
1142 sec) and after incubation with $CSC^{mClover}$ variants (370 sec). Tubes were imaged by spin-
1143 ning disc confocal microscopy at 0.5 Hz throughout the experiment. Scale bars: 2 µm
1144 **d.** Kymographs of the tubes shown in c.
1145
1146 **Suppl. Figure 5. Effect of vps35 dimerization mutants on the localization of Vps10,**
1147 **Vps17 and Vps29 in yeast cells.**
1148 **a**. Vps35 expression levels. Cells expressing the indicated VPS35 alleles as TAP fusion
1149 proteins were grown in YPD to mid-logarithmic phase. Whole-cell extracts were analyzed
1150 by SDS-PAGE and Western blotting against the TAP tag.
1151 **b, c.** Colocalization of $Vps10^{yEGFP}$ with yomCherry fusions of (b) Vps29 and (c) Vps17. All
1152 tags were introduced at the genomic locus, generating C-terminal fusions as the sole
1153 source of the respective proteins. Cells had been harvested in logarithmic growth (OD_{600nm}
1154 between 0.8 and 1.0), concentrated in their medium by a short spin and immediately im-
1155 aged by spinning disc confocal microscopy. Arrowheads indicate co-localization of retro-
1156 mer subunits with $Vps10^{yEGFP}$. The merge includes a brightfield image to indicate the cell
1157 boundaries.
1158 **d.** Quantification of $Vps10^{yEGFP}$ dots colocalizing with $Vps17^{mCherry}$ in cells from c. Quantifi-
1159 cation was done with the Nikon analysis software NIS-Elements. Statistical significance
1160 was assessed with a two-tailed t-test. **** $P < 0.0001$.
1161
1162 **Suppl. Figure 6. Dominant negative effect of hVPS35 variants on GLUT1 sorting in**
1163 **HK2 cells**
1164 **a.** HK2 cells were transfected with a plasmid carrying the indicated variants of $hVPS35^{GFP}$,
1165 or with an empty plasmid, and cultivated for 24h. They were fixed, stained with antibody to
1166 GLUT1 (red) and with DAPI (blue) and analyzed by confocal microscopy. The cells were
1167 not detergent permeabilized. Scale bar: 10 µm
1168 **b.** Quantification of GLUT1 fluorescence in the cells from a was performed as in Fig. 9c.
1169 **c.** Expression of Vps35 variants in cells from a was analyzed by SDS-PAGE and Western
1170 blot against Vps35. Tubulin served as loading control.

1171 **d.** Quantification of the Vps35/tubulin ratio in cells from a. Data stems from three inde-
1172 pendent experiments and show the mean. NS: not significant according to a two tailed t-
1173 test (p>0.01).
1174
1175 **Suppl. Figure 7: Effect of VPS35 variants on the size of LAMP1 compartments.**
1176 **a**. Effect of VPS35 knockdown. HK2 cells were treated with siRNA targeting VPS35 or with
1177 mock siRNA. The cells were fixed and immuno-stained with anti-LAMP1 antibody and
1178 DAPI and imaged by confocal microscopy. Representative images are shown. Scale bar:
1179 10 µm. Arrowheads point to examples of enlarged LAMP1-compartments.
1180 **b.** Effect of VPS35 variants. Vps35 knock-down cells were transfected with a plasmid ex-
1181 pressing siRNA-resistant wildtype or mutant forms of $VPS35^{GFP}$, or with an empty plasmid.
1182 Cells were fixed, immuno-stained with anti-LAMP1 and DAPI and imaged by confocal mi-
1183 croscopy. Scale bar: 10 µm. Arrowheads point to examples of enlarged LAMP1-compart-
1184 ments.
1185
1186
1187
1188
1189
1190
1191
1192
1193
1194
1195
1196
1197

1198 **Supplementary Tables**

1199 **Suppl. Table 1 – strains used in this study**

Strain	Genotype	Reference
CUY105	*MATa his3Δ200 leu2Δ0 met15Δ0 trp1Δ63 ura3Δ0*	(Purushothaman & Ungermann, 2018; Purushothaman *et al*, 2017)
CUY100	*MATalpha his3Δ200 leu2Δ0 lys2Δ0 met15Δ0 trp1Δ63 ura3Δ0*	(Purushothaman & Ungermann, 2018; Purushothaman *et al*, 2017)
CUY9228	CUY105, *VPS5pr::natNT1-GAL1pr VPS17pr::kanMX-GAL1pr VPS5::TAP-URA3 vps35::HIS3*	(Purushothaman & Ungermann, 2018; Purushothaman *et al*, 2017)
CUY9495	*CUY100, VPS26pr::HIS3-GAL1pr VPS29pr::natNT2-GAL1pr VPS35pr::hphNT1-GAL1 VPS35::TAP-kanMX vps5::TRP1 vps17::LEU2*	(Purushothaman & Ungermann, 2018; Purushothaman *et al*, 2017)
CUY9711	*CUY105, VPS5pr::natNT1-GAL1pr VPS17pr::kanMX-GAL1pr VPS5::TAP-URA3 vps35::HIS3 VPS17::GFP-hphNT1*	(Purushothaman & Ungermann, 2018; Purushothaman *et al*, 2017)
CUY9932	*CUY105, VPS26pr::HIS3-GAL1pr VPS29pr::natNT2-GAL1pr VPS35pr::hphNT1-GAL1 VPS29*-mClover*::kan VPS26::TAP-URA3 vps5Δ::TRP1*	(Purushothaman & Ungermann, 2018; Purushothaman *et al*, 2017)
CUY9935	*CUY105, VPS26pr::HIS3-GAL1pr VPS29pr::natNT2-GAL1pr VPS35pr::hphNT1-GAL1pr VPS29*-mCherry*::kan VPS26::TAP-URA3 vps5Δ::TRP1*	(Purushothaman & Ungermann, 2018; Purushothaman *et al*, 2017)
NG403	CUY9932, Vps35 E681A/E682A/D686A/K726E/K729E/K730E (AAA3KE)	This study
NG406	CUY9932, Vps35 D671A/L772A/K726A/R775A (PISA)	This study
4510	*BY4741 WT vps10yeGFP::His*	This study

4511	*BY4741 vps35Δ::KanMX Vps10yeGFP::spHIS5*	This study
4512	*BY4741 VPS35PISA::LEU Vps10yeGFP::spHIS5*	This study
4513	*BY4741 VPS35AA3KE::LEU Vps10yeGFP::spHIS5*	This study
4643	*BY4741 WT VPS10yeGFP::spHIS5 VPS17yomCherry::CaURA3*	This study
4645	*BY4741 VPS35PISA::LEU VPS10yeGFP::spHIS5 VPS17yomCherry::CaURA3*	This study
4646	*BY4741 VPS35AA3KE::LEU VPS10yeGFP::spHIS5 VPS17yomCherry::CaURA3*	This study
4647	*BY4741 WT VPS10yeGFP::spHIS5 VPS29yomCherry::CaURA3*	This study
4649	*BY4741 VPS35PISA::LEU VPS10yeGFP::spHIS5 VPS29yomCherry::CaURA3*	This study
4650	*BY4741 VPS35AA3KE::LEU VPS10yeGFP::spHIS5 VPS29yomCherry::CaURA3*	This study

Suppl. Table 2 – primers used in this study

Fluorescent protein taging	

Pep1 286 Pep1 Ctag F C Terminal tagging with pKT F5	CGACAGGCCTGATTCTACAGCGCCATCTAACGAAAACCAGcggatccccgggttaattaa
Pep1 287 Pep1 Ctag R C Terminal tagging with pKT R3	GTATATGGAATTATCTACTCTATGTAAAGTAATCTCTCTAgaattcgagctcgtttaaac
VPS29 54-VPS29 Cterm pKT F C Terminal tagging with pKT F5	TGGAGAAGTGAAGGTCGATAAAGTGGTTTATGAAAAGGAAggtgacggtgctggttta
VPS5 55-VPS29 Cterm pKT R C Terminal tagging with pKT R3	GACATCATAGAAATGCATAAAAATGAAAATGGCTACCCTAtcgatgaattcgagctcg
YD276_Vps17 F5 C Terminal tagging with pKT F5	ACTGAATGCGCGCCATGCTGCTTCACTTTTGGGCATGTCCACTAAAGGTGACGGTGCTGGTTTA
YD277_Vps17 R3 C Terminal tagging with pKT R3	GATCACCTTGTTCAAAGGTATGAATTTTCTACTTTATATACGTATCGATGAATTCGAGCTCG
Vps35 Cterm amplification for fusion PCR	
vps35-mut-F	GACATCTTAATGGATAGAGAAGTG
35-Term-2LEU-R	CTTACGATACCTGAGTATTCCCACAGTTAACTGCGGTCAAGATATTTCTGGCCAAAATGATACTTTACCTGATGT
LEU2 amplification for fusion PCR	
Leu2-F	GAAATATCTTGACCGCAGTTAACTGTGG
LEU2-R-35homo	GCTTGGTGAATTTAAGAGCGAAGGGAAAGCAAAGATTATATATTAAATTCGGACTTAAACTCCATCAAATGGTCAGGTC

1203

1204

1205

1206

Figure 1

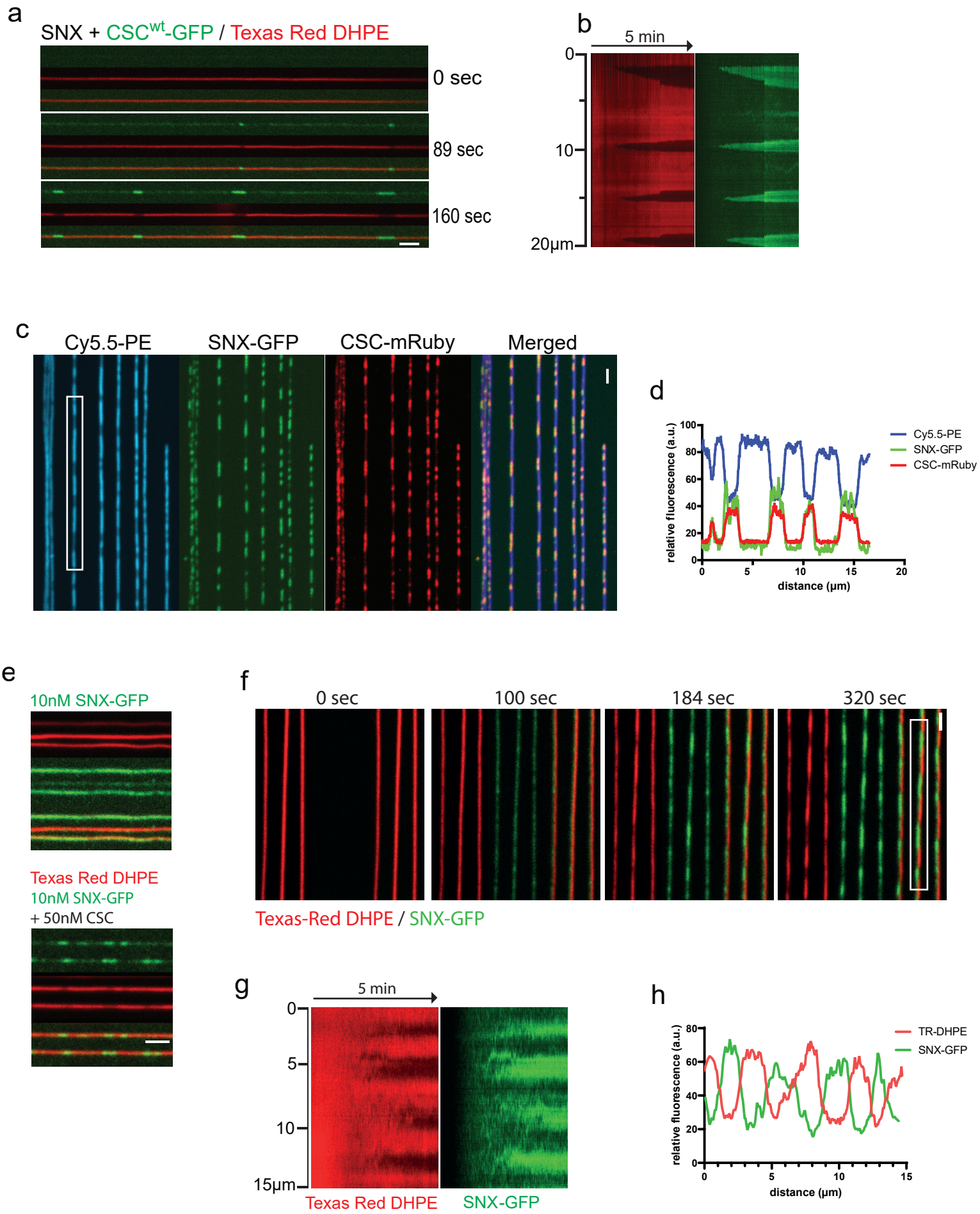
a
SNX + CSC^{wt}-GFP / Texas Red DHPE
0 sec
89 sec
160 sec
b
5 min
0
10
20µm
c
Cy5.5-PE
SNX-GFP
CSC-mRuby
Merged
d
relative fluorescence (a.u.)
distance (µm)
Cy5.5-PE
SNX-GFP
CSC-mRuby
e
10nM SNX-GFP
Texas Red DHPE
10nM SNX-GFP
+ 50nM CSC
f
0 sec
100 sec
184 sec
320 sec
Texas-Red DHPE / SNX-GFP
g
5 min
0
5
10
15µm
Texas Red DHPE
SNX-GFP
h
relative fluorescence (a.u.)
distance (µm)
TR-DHPE
SNX-GFP

Figure 2

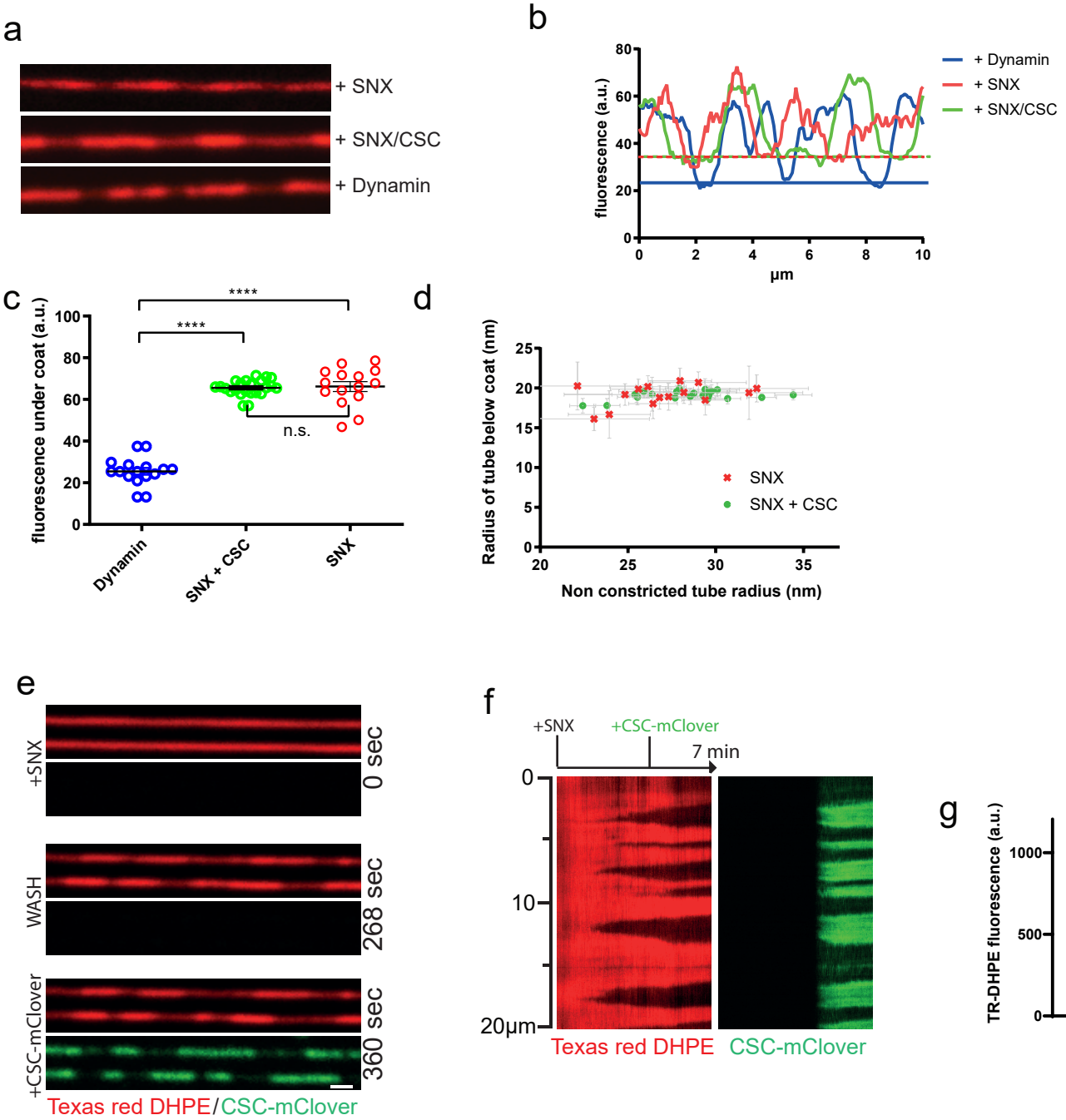
a
+ SNX
+ SNX/CSC
+ Dynamin
b
fluorescence (a.u.)
µm
+ Dynamin
+ SNX
+ SNX/CSC
c
fluorescence under coat (a.u.)
****
****
n.s.
Dynamin
SNX + CSC
SNX
d
Radius of tube below coat (nm)
Non constricted tube radius (nm)
SNX
SNX + CSC
e
+SNX
0 sec
WASH
268 sec
+CSC-mClover
360 sec
Texas red DHPE/CSC-mClover
f
+SNX
+CSC-mClover
7 min
20µm
Texas red DHPE
CSC-mClover
g
TR-DHPE fluorescence (a.u.)
ns
-CSC
+CSC

Figure 3

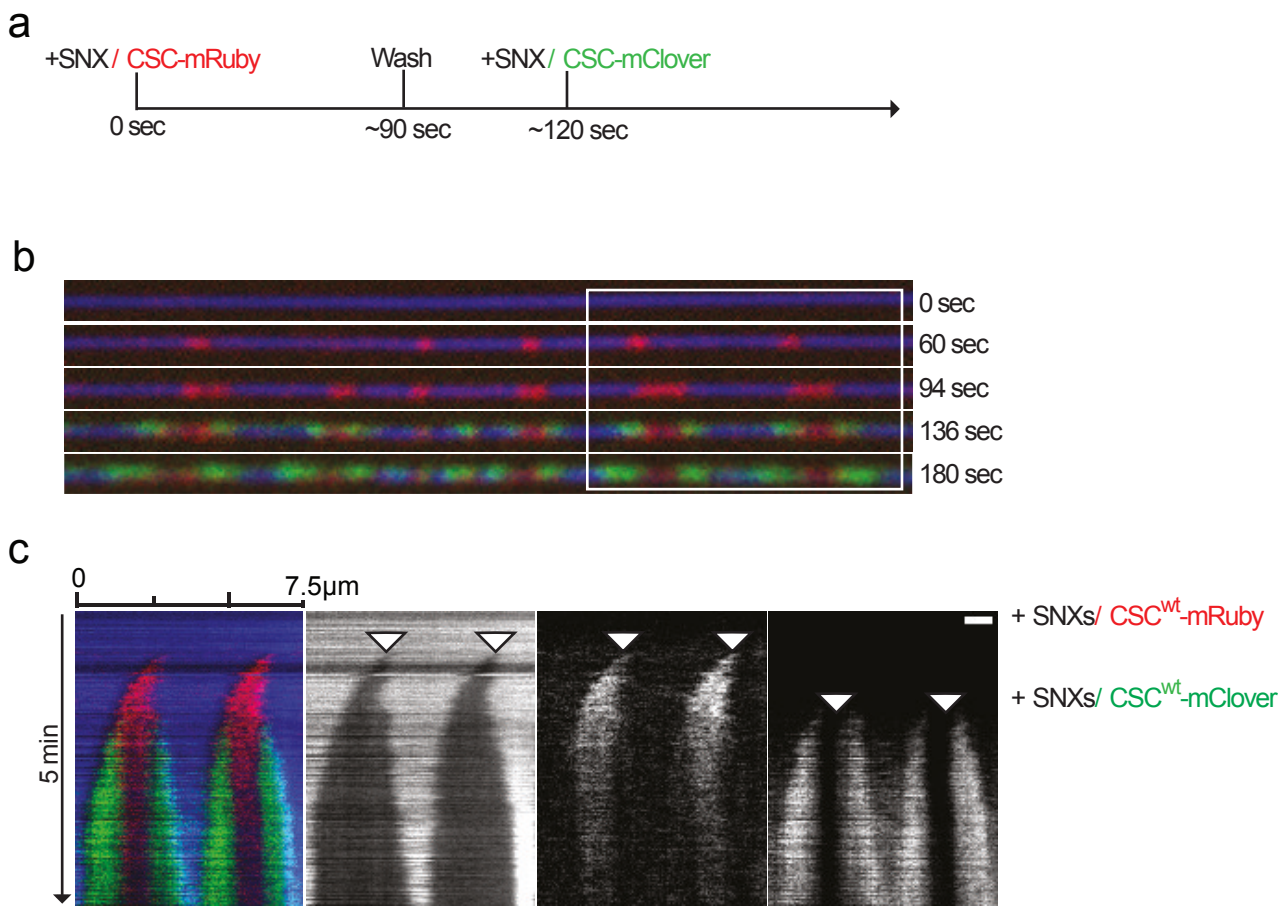
a
+SNX / CSC-mRuby
Wash
+SNX / CSC-mClover
0 sec
~90 sec
~120 sec
b
0 sec
60 sec
94 sec
136 sec
180 sec
c
0
7.5µm
5 min
+ SNXs/ CSCwt-mRuby
+ SNXs/ CSCwt-mClover

figure 4

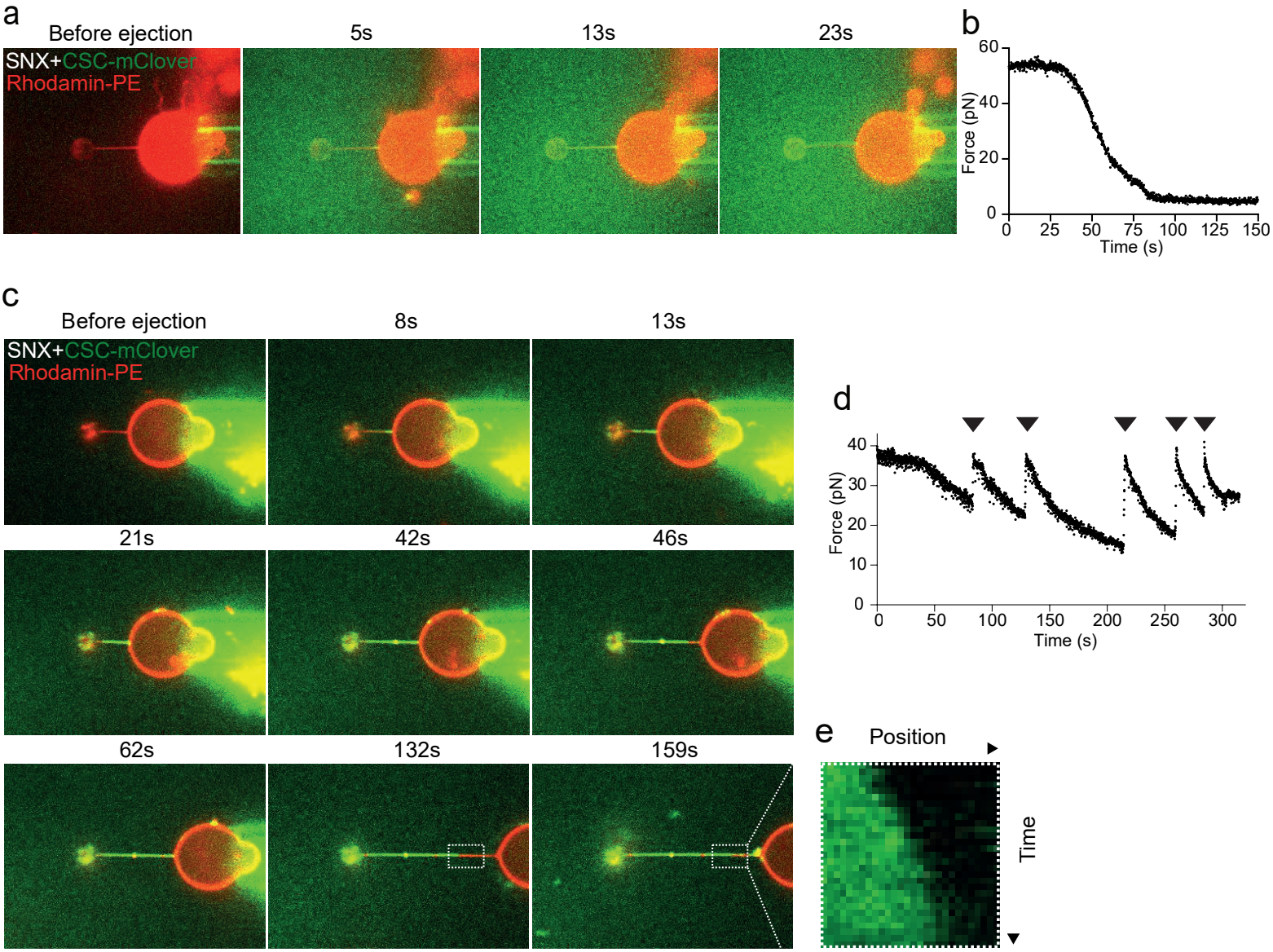
a
Before ejection
5s
13s
23s
SNX+CSC-mClover
Rhodamin-PE
b
Force (pN)
Time (s)
c
Before ejection
8s
13s
SNX+CSC-mClover
Rhodamin-PE
21s
42s
46s
62s
132s
159s
d
Force (pN)
Time (s)
e
Position
Time

Figure 5

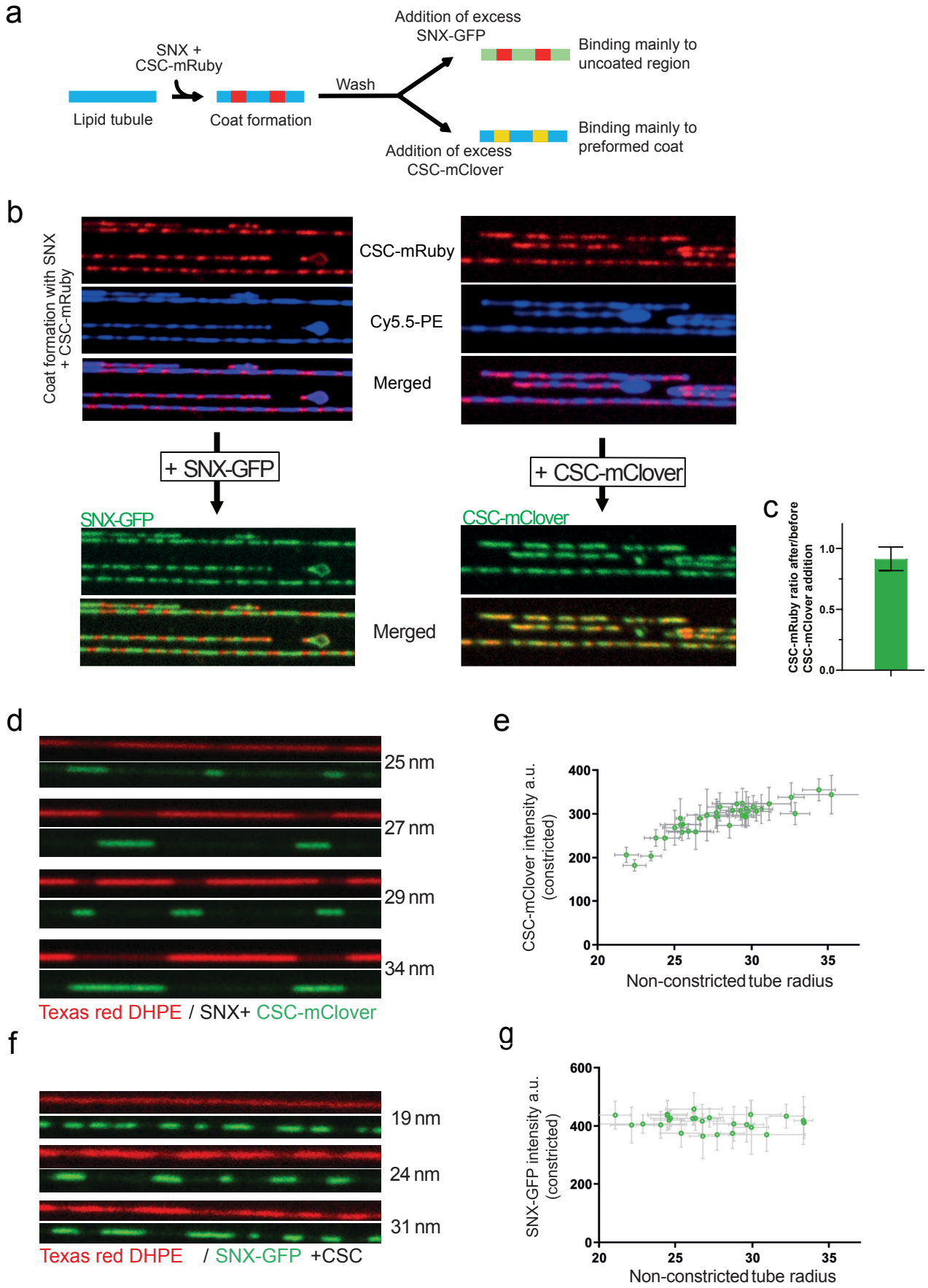
a
SNX +
CSC-mRuby
Lipid tubule
Coat formation
Wash
Addition of excess
SNX-GFP
Binding mainly to
uncoated region
Addition of excess
CSC-mClover
Binding mainly to
preformed coat
b
Coat formation with SNX
+ CSC-mRuby
CSC-mRuby
Cy5.5-PE
Merged
+ SNX-GFP
+ CSC-mClover
SNX-GFP
Merged
CSC-mClover
c
CSC-mRuby ratio after/before
CSC-mClover addition
1.0
0.5
0.0
d
25 nm
27 nm
29 nm
34 nm
Texas red DHPE / SNX+ CSC-mClover
e
CSC-mClover intensity a.u.
(constricted)
400
300
200
100
0
20
25
30
35
Non-constricted tube radius
f
19 nm
24 nm
31 nm
Texas red DHPE / SNX-GFP +CSC
g
SNX-GFP intensity a.u.
(constricted)
600
400
200
0
20
25
30
35
Non-constricted tube radius

Figure 6

a

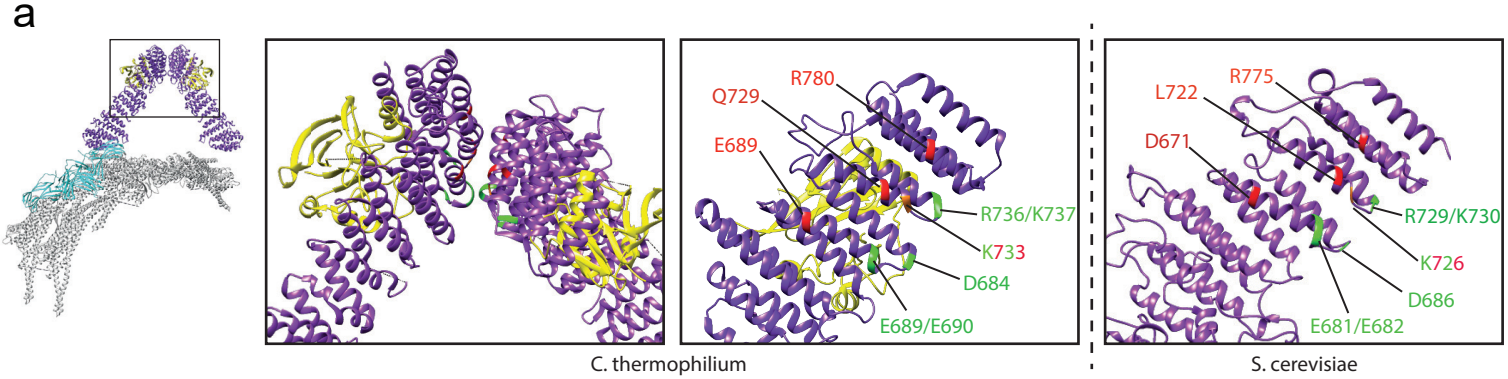

b

```
S.cerevisiae        664   QLNEISYDFFSQAFTIFEESLSDSKTQLQALIYIAQSLQKTRSLYKEAYYDSLIVRCTLHGSKLLKKQDQCRAVYLCSH   742
C.thermophilum      682   EFEEVAYEFFAQAFTVYEESISDSKAQFQAVCVIASALHRTRN-FGRENYDTLITKCAQHASKLLRKPDQCRAVYLASH   749
D.discoideum        616   SR---VKELAIKALLIFQEDIADFKAQVMALQLLISTLNSLSI-PNEEIYESLAAQTIKQASRLLLPQDQAKLISTCSH   680
D.melanogaster      606   NHETVAYEFMTQAFSLYEDEISDSKAQLAAITLIMSTFEQMSC-FGEENAEPLRTNCALAASKLLKKPDQCRGVVACAA   683
M.musculus          598   NHETVAYEFMSQAFSLYEDEISDSKAQLAAITLIIGTFERMKC-FSEENHEPLRTQCALAASKLLKKPDQGRAVSTCAH   675
H.sapiens           598   NHETVAYEFMSQAFSLYEDEISDSKAQLAAITLIIGTFERMKC-FSEENHEPLRTQCALAASKLLKKPDQGRAVSTCAH   675
                          .      ::  :*: :::: .::* *:*. *:  :  ::.       .   : * ..    .*:**   ** : :  .:

Saccharomyces       LWWATEISNIGEEEGITDNFYRDGKRVLECLQRSLRVADSIMDNEQSCELMVEILNRCLY   802
C.thermophilu       LWWATPIAARGETE--DTELYRDGKRVLECLQRALRVADSCMETATSIELFVEILDRYVY   807
D.discoideum        LFWVDNPS----------RQYQNPDSVLQALKKALSIISNESSPGL--GTFVDILNECLF   728
D.melanogaster      LFWSGKQ---------NGEEMRDEKRTLDCLKKGARIASQCLDTGVQVQLYVELLNHYLF   734
M.musculus          LFWSGRNT----DK--NGEELHGGKRVMECLKKALKIANQCMDPSLQVQLFIEILNRYIY   729
H.sapiens           LFWSGRNT----DK--NGEELHGGKRVMECLKKALKIANQCMDPSLQVQLFIEILNRYIY   729
                    *:*               .  :. . .::.*::.  : ..  .        :::*:. ::
```

AAA3KE
PISA

c

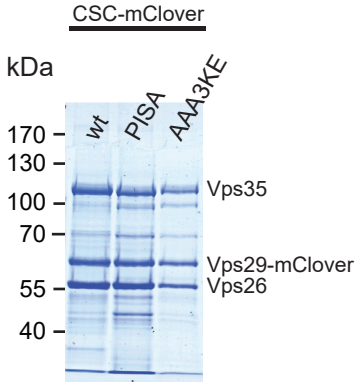

d

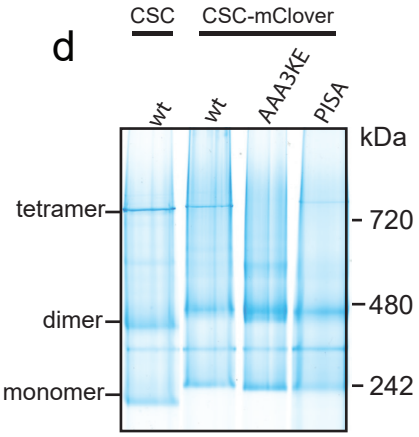

Figure 7

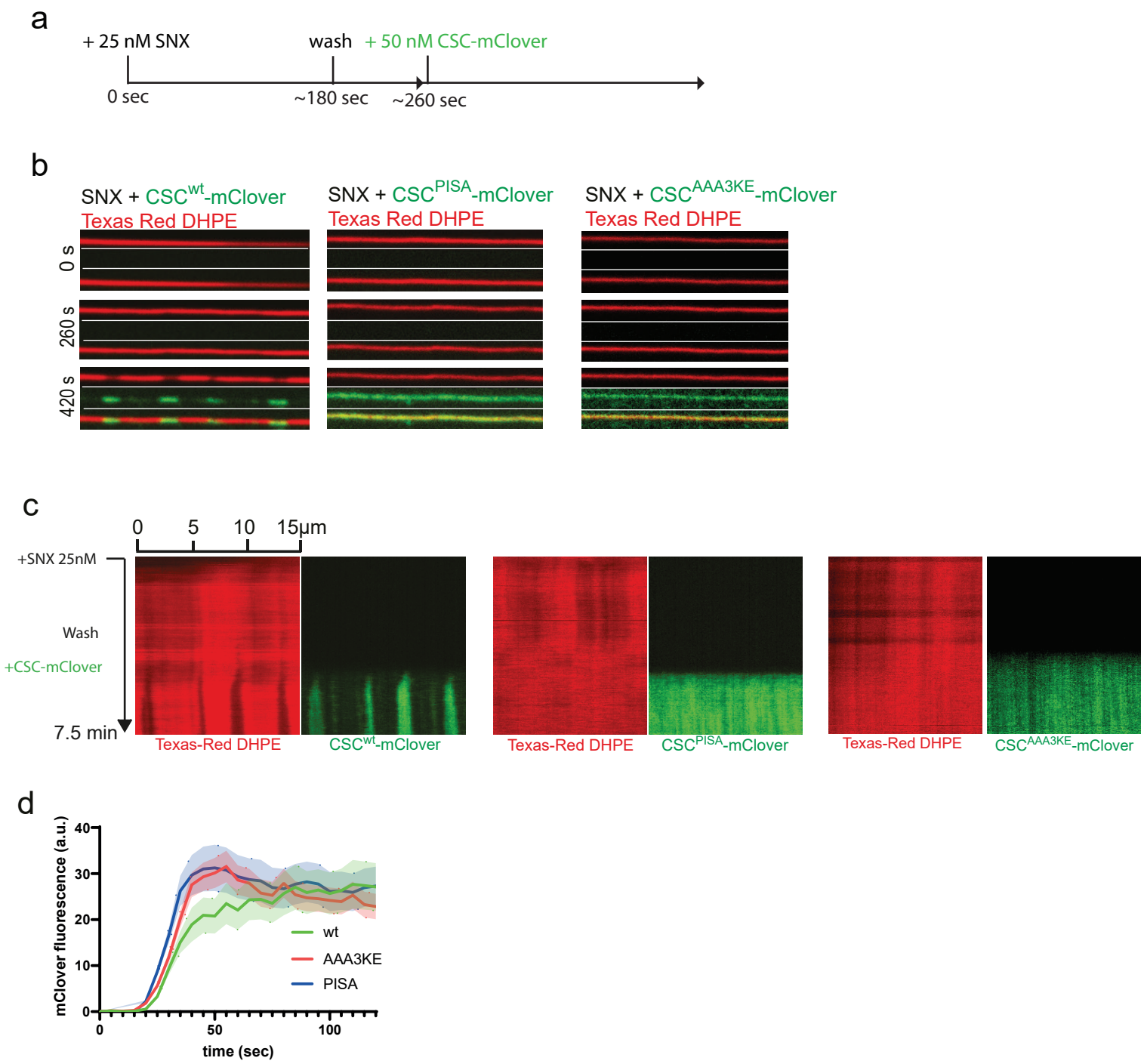
a
+ 25 nM SNX
wash
+ 50 nM CSC-mClover
0 sec
~180 sec
~260 sec
b
SNX + CSCwt-mClover
Texas Red DHPE
SNX + CSCPISA-mClover
Texas Red DHPE
SNX + CSCAAA3KE-mClover
Texas Red DHPE
0 s
260 s
420 s
c
0
5
10
15µm
+SNX 25nM
Wash
+CSC-mClover
7.5 min
Texas-Red DHPE
CSCwt-mClover
Texas-Red DHPE
CSCPISA-mClover
Texas-Red DHPE
CSCAAA3KE-mClover
d
mClover fluorescence (a.u.)
40
30
20
10
0
0
50
100
time (sec)
wt
AAA3KE
PISA

Figure 8

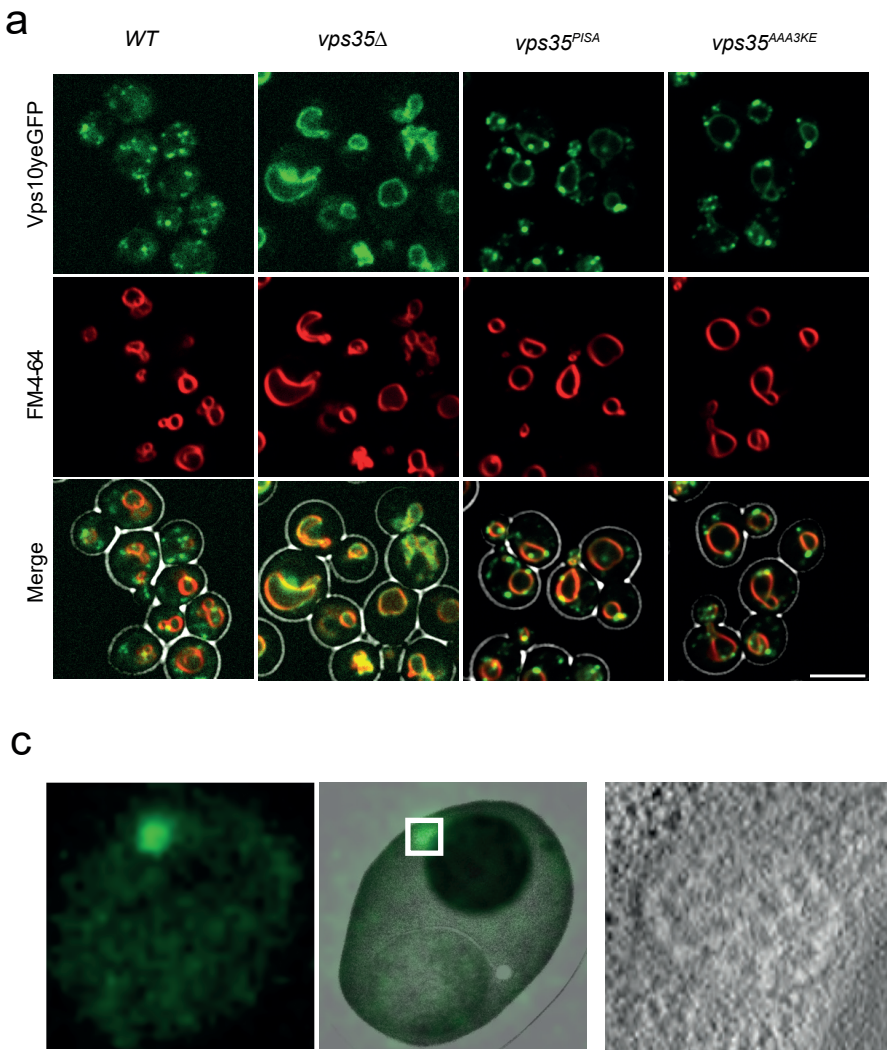
a
WT
vps35Δ
vps35PISA
vps35AAA3KE
Vps10yeGFP
FM4-64
Merge
b
Vps10/FM4-64 colocalization
Pearson's correlation coefficient
1.0
0.8
0.6
0.4
0.2
0.0
****
****
****
n.s
wt
vps35Δ
vps35PISA
vps35AAA3KE
c

Figure 9

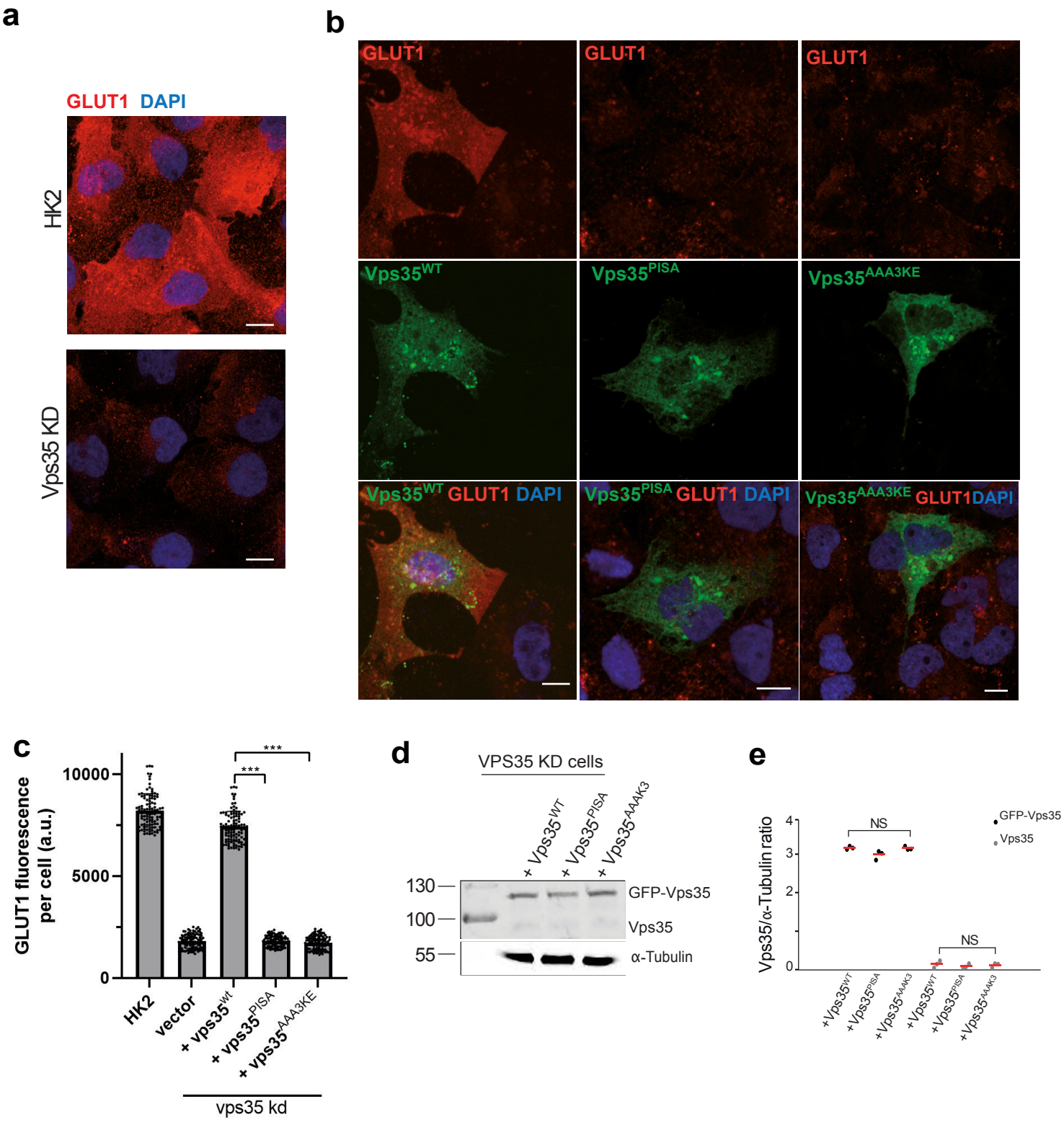
a
GLUT1 DAPI
HK2
Vps35 KD
b
GLUT1
GLUT1
GLUT1
Vps35WT
Vps35PISA
Vps35AAA3KE
Vps35WT GLUT1 DAPI
Vps35PISA GLUT1 DAPI
Vps35AAA3KE GLUT1DAPI
c
GLUT1 fluorescence per cell (a.u.)
10000
5000
0
***
***
HK2
vector
+ vps35wt
+ vps35PISA
+ vps35AAA3KE
vps35 kd
d
VPS35 KD cells
+ Vps35WT
+ Vps35PISA
+ Vps35AAAK3
130
100
55
GFP-Vps35
Vps35
α-Tubulin
e
Vps35/α-Tubulin ratio
4
3
2
0
NS
NS
GFP-Vps35
Vps35
+Vps35WT
+Vps35PISA
+Vps35AAAK3
+Vps35WT
+Vps35PISA
+Vps35AAAK3

Supplementary figure 1

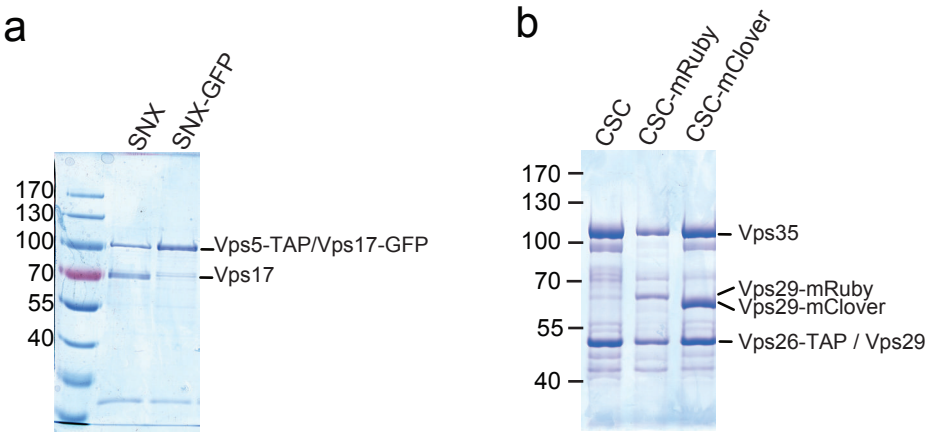

Supplementary figure 2

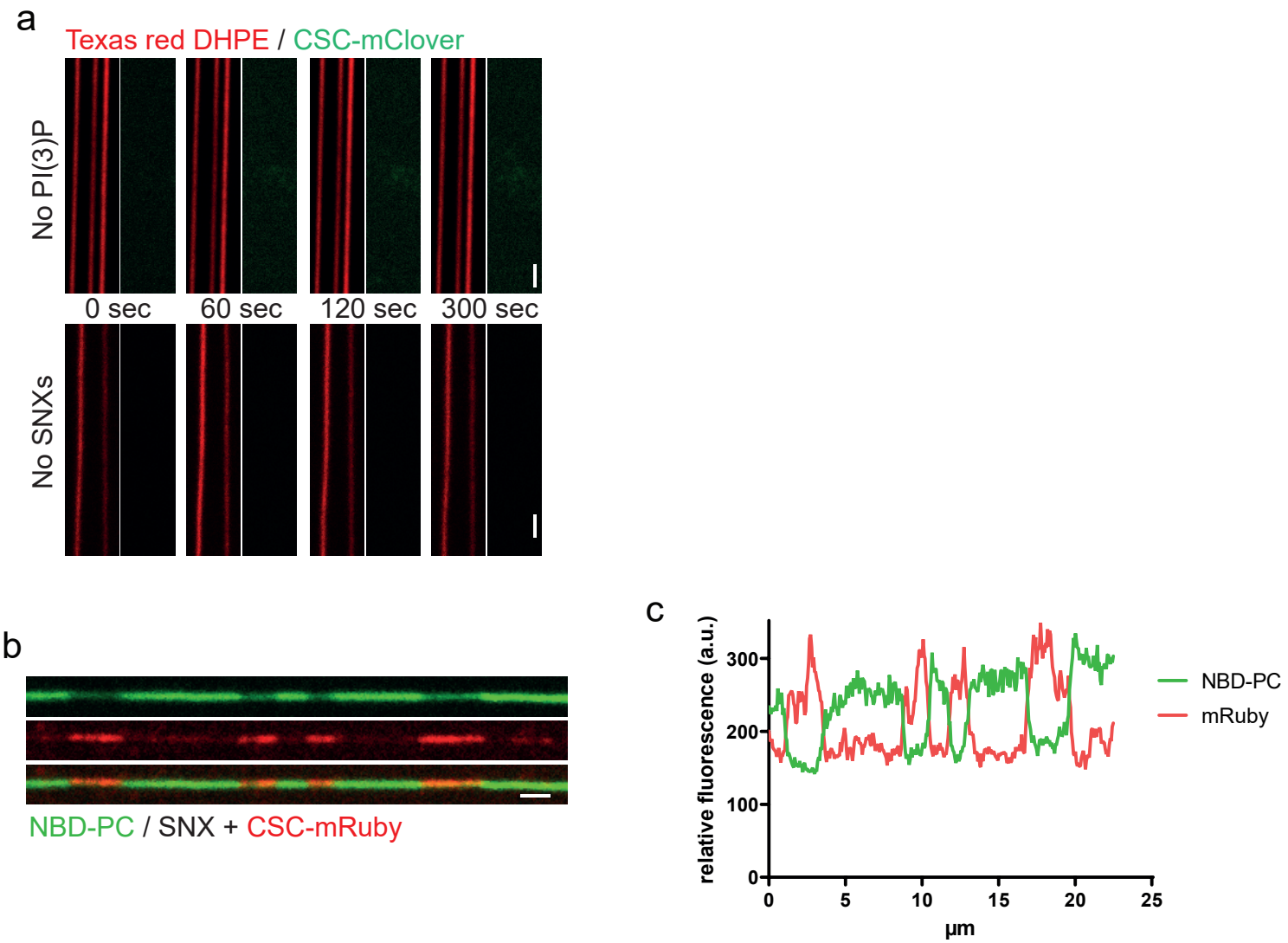

Supplementary figure 3

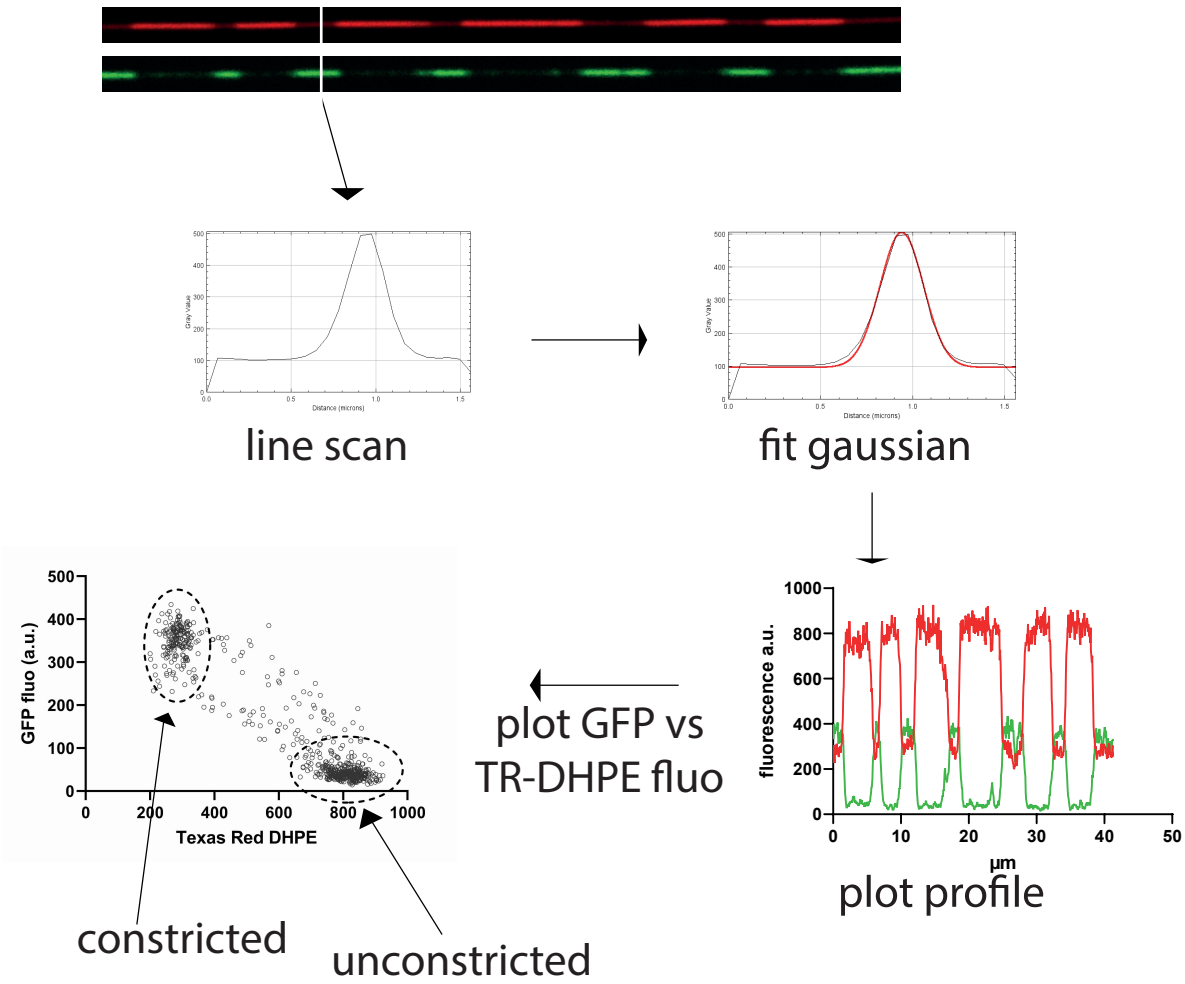

Supplementary figure 4

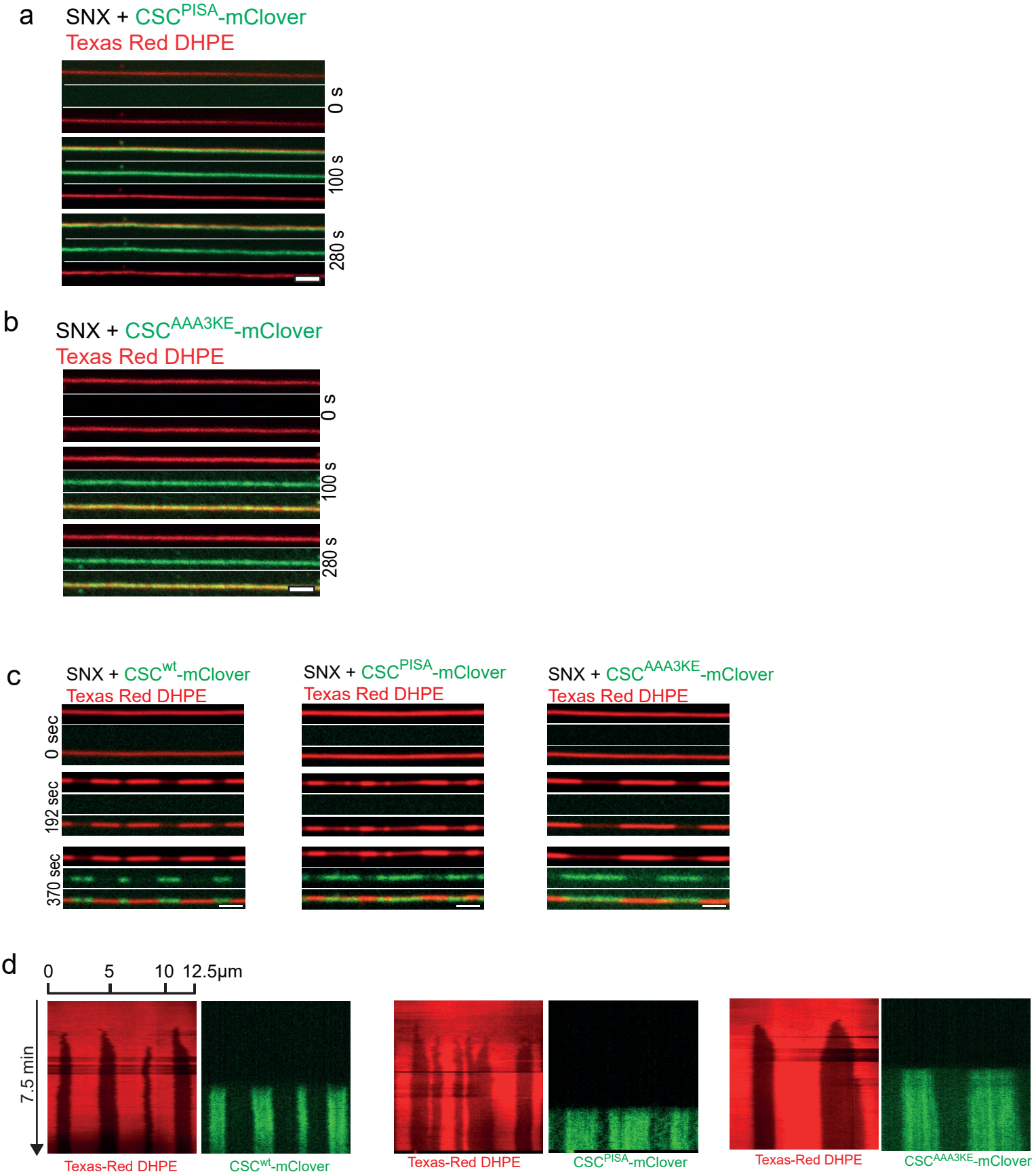

Supplementary figure 5

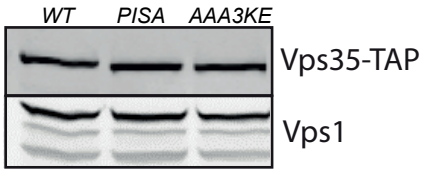

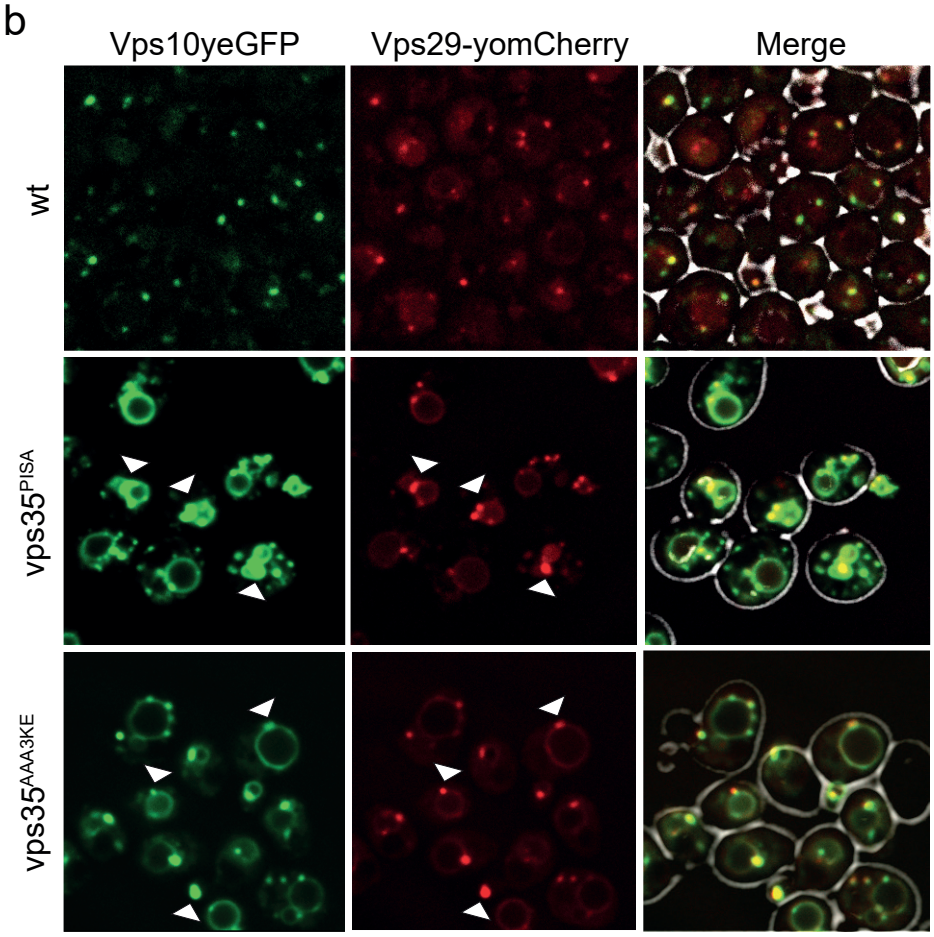

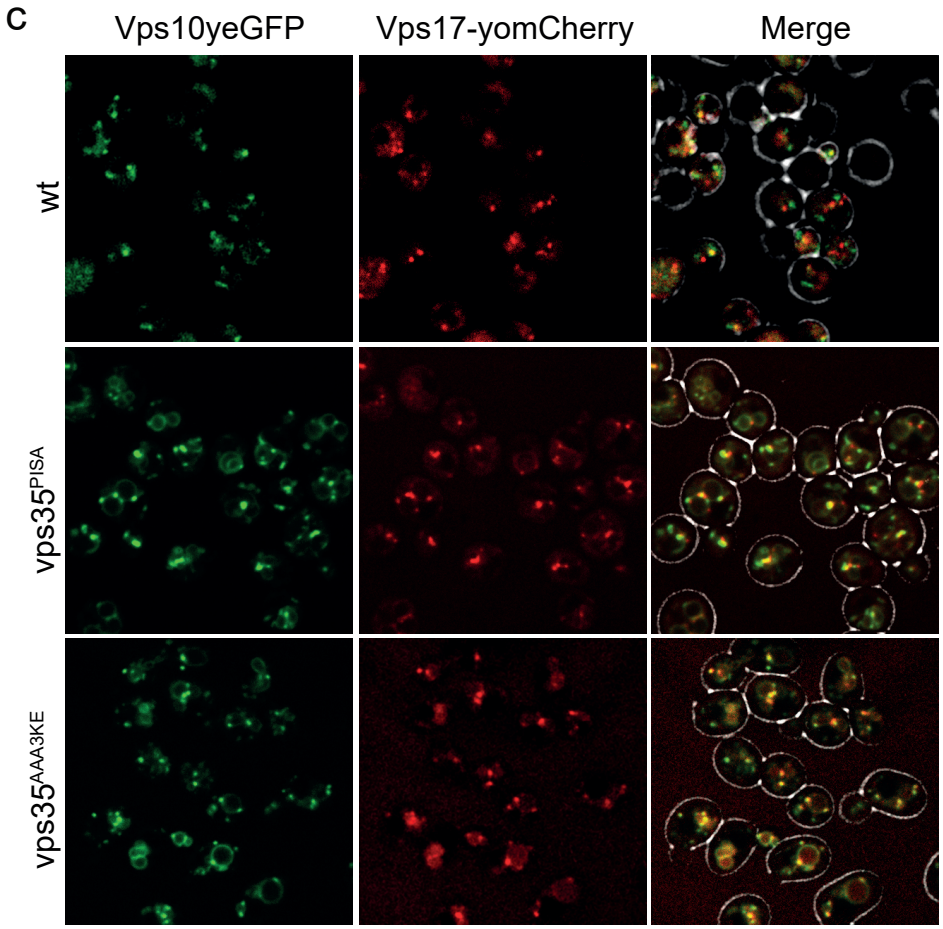

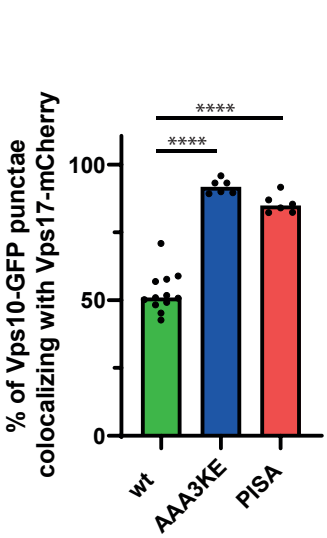

Supplementary figure 6

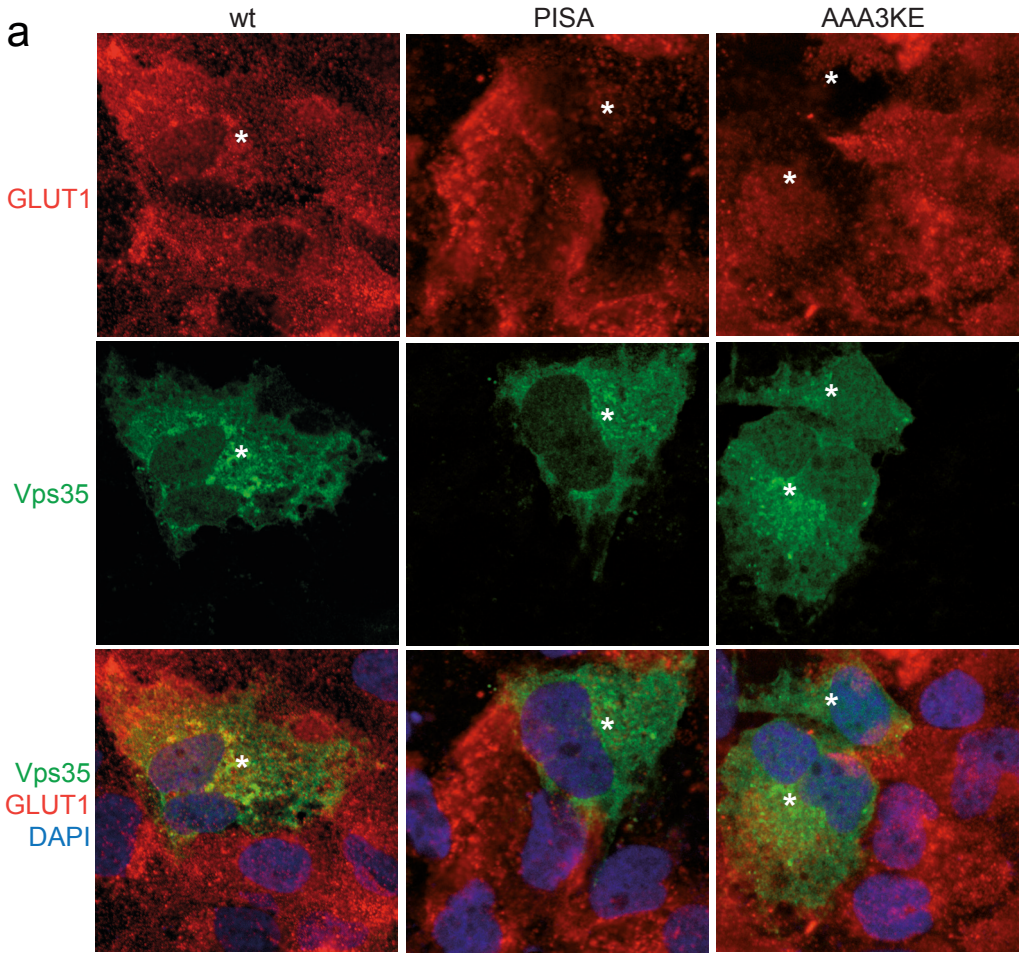

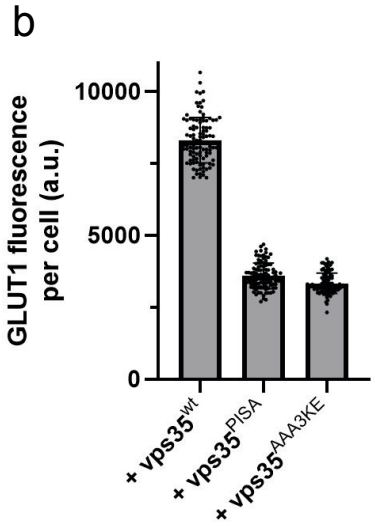

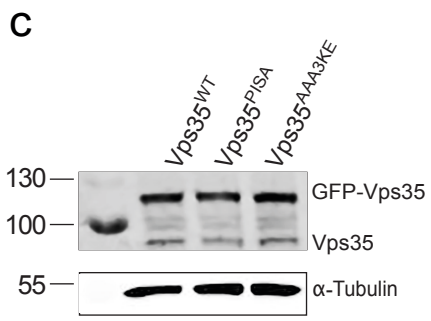

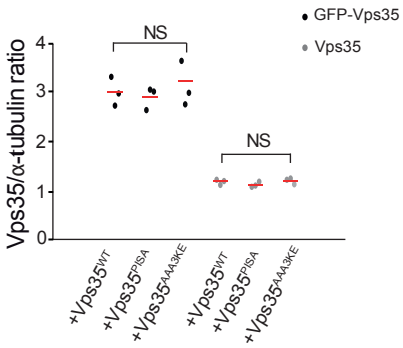

Supplementary figure 7